Subgrain rotation recrystallization during shearing: insights from full-field numerical simulations of halite polycrystals

E. Gomez-Rivas[1], A. Griera[2], M. -G. Llorens[3],

P. D. Bons[3], R. A. Lebensohn[4], and S. Piazolo[5]

[1]School of Geosciences, King's College, University of Aberdeen, Aberdeen AB24 3UE, United Kingdom

[2]Departament de Geologia, Universitat Autònoma de Barcelona, 08193 Bellaterra (Cerdanyola del Vallès), Spain

[3]Department of Geosciences, Eberhard Karls University of Tübingen, Wilhelmstr. 56, 72074 Tübingen, Germany

[4]Materials Science and Technology Division, Los Alamos National Laboratory, Los Alamos NM 87545, USA

[5]School of Earth and Environment, University of Leeds, Leeds LS2 9JT, United Kingdom

Corresponding author: Enrique Gomez-Rivas (e.gomez-rivas@abdn.ac.uk)

Key Points:

- Full-field numerical simulations of subgrain rotation recrystallization, able to reproduce experiments, are presented for first time

- Intracrystalline recovery strongly decreases grain size reduction but does not change crystal preferred orientations

- Mean subgrain misorientations can be used as a strain gauge for polycrystals undergoing recrystallization, following a universal law

Abstract

We present, for the first time, results of full-field numerical simulations of subgrain rotation recrystallization of halite polycrystals during simple shear deformation. The series of simulations show how microstructures are controlled by the competition between (i) grain size reduction by creep by dislocation glide and (ii) intracrystalline recovery encompassing subgrain coarsening (SGC) by coalescence through rotation and alignment of the lattices of neighboring subgrains. A strong grain size reduction develops in models without intracrystalline recovery, as a result of the formation of high-angle grain boundaries when local misorientations exceed 15°. The activation of subgrain coarsening associated with recovery decreases the stored strain energy and results in grains with low intracrystalline heterogeneities. However, this type of recrystallization does not significantly modify crystal preferred orientations. Lattice orientation and grain boundary maps reveal that this full-field modelling approach is able to successfully reproduce the evolution of dry halite microstructures from laboratory deformation experiments, thus opening new opportunities in this field of research. We demonstrate how the mean subgrain boundary misorientations can be used to estimate the strain accommodated by dislocation glide using a universal scaling exponent of about 2/3, as predicted by theoretical models. In addition, this strain gauge can be potentially applied to estimate the intensity of intracrystalline recovery, associated with temperature, using quantitative crystallographic analyses in areas with strain gradients.

1 Introduction

Understanding rock deformation microstructures is essential to unravel tectonic processes and to predict physical properties of crustal and mantle rocks. Polycrystalline aggregates typically develop crystal preferred orientations (CPO) and may lead to strongly anisotropic behavior when they are deformed by dislocation creep [*Urai et al.*, 1986; *Passchier and Trouw*, 2005]. Halite (NaCl) is a widely used mineral to understand the behavior of rocks deformed in the ductile regime [*e.g., Carter et al.*, 1982; *Stone et al.*, 2004; *Bourcier et al.*, 2013]. It has very special properties, since it is nearly incompressible, highly soluble, has a very low permeability, and can flow ductilly in the solid state under relatively low stresses. Therefore, it is widely used for deformation and recrystallization experiments, and is an accepted analogue material for silicates that deform ductilly at much higher temperatures and pressures [e.g., *Guillope and Poirier*, 1979]. At low temperature and dry conditions halite deforms by dislocation creep, with subgrain rotation [SGR; e.g., *Urai et al.*, 1986; *Trimby et al.*, 2000] being the dominant recrystallization mechanism [regime 2 of *Hirth and Tullis*, 1992]. This results in an anisotropic behavior with the development of strong intracrystalline heterogeneities. SGR is linked to the formation of subgrain boundaries as a consequence of strain, and is also associated with the reduction of free energy by the activation of intracrystalline processes that result in the reorganization of subgrains (recovery) [e.g., *Halfpenny et al.*, 2006; *Karato*, 2012]. Two main processes influence the formation of subgrain boundaries: (i) annihilation of dislocations of opposite signs, assisted by climb, and (ii) polygonization, which consists on the alignment of dislocations [*Humphreys and Hatherly*, 2004; *Borthwick and Piazolo*, 2010]. In such a situation, dislocations move and interact to form low-angle subgrain boundaries (LAGB), leading to an increase in misorientation between subgrains [*Urai et al.*, 1986]. Progressive strain increases this misorientation angle until a critical value is reached, allowing the subgrains to become new grains as their boundaries achieve high angles (HAGB). This critical angle ranges between 10º and 15º, when the distances between dislocations are similar to the atomic ones [*Karato*, 2012]. This process results in a strong grain size reduction with increasing

deformation and the formation of recrystallized grains that tend to have a size similar to that of the subgrains.

Several studies have analyzed the development of low-angle boundaries and how misorientations are related to strain. Two types of dislocation boundaries are distinguished [*Kuhlmann-Wilsdorf and Hansen*, 1991; *Pantleon*, 2001]: incidental dislocation boundaries (IDBs), which result from statistical mutual trapping of dislocations, and geometrically necessary boundaries (GNBs), which form due to the activation of different sets of slip systems or the different activity of the same set of slip systems on each side of the boundary. *Hughes et al.* [1997; 1998; 2003] proposed a material-independent universal scaling behavior between the average misorientation (θ_{av}) of the system and the natural strain (ε) using metal deformation experiments. *Pantleon* [1997; 1998; 2001] and *Sethna and Coffman* [2003] confirmed these scaling laws and provided explanations for the misorientation distributions and their scaling laws, focusing on metals. *Pennock et al.* [2005] proposed a new approach, in which misorientations are measured on a grain basis, and obtained a slightly different scaling law. If this universal scaling also applies to rocks, this strain gauge can be a useful tool, since it allows the estimation of strain by measuring misorientations from deformed samples with electron backscatter diffraction analysis (EBSD). However, this method has only been applied to cases of coaxial deformation, and the interplay between dislocation glide/creep and synchronous recovery of intracrystalline defects or post-deformation annealing can result in a substantial modification of the microstructure and the reduction of subgrain misorientations associated with the decrease of free energy (i.e., boundary and strain stored energies). This process can strongly affect microstructures in halite and other materials [*Borthwick and Piazolo*, 2010], thus potentially hindering the use of subgrain misorientations as a strain gauge.

Numerical simulation is a very useful tool that can complement the study of natural and experimental samples, because it allows analysis of the effects of single or coupled deformation processes in a wide range of deformation scenarios and for systems with variable material properties. Moreover, simulations can overcome some of the limitations of experiments, because variable sample sizes can be studied, and also high finite strain can be achieved at low strain rates. The numerical evolution of textures and crystallographic preferred orientations (CPOs) of polycrystalline aggregates has been widely investigated using kinematic [e.g., D-REX, *Kaminsky and Ribe*, 2001] and self-consistent approaches, such as the viscoplastic self-consistent formulation (VPSC) [*Wenk et al.*, 1989; *Lebensohn et al.*, 2003; *Liu et al., 2005*]. The VPSC method models the reorientation of grains through intracrystalline slip and grain interaction assuming a homogenous equivalent matrix. It adequately predicts lattice rotations depending on the slip system activity, and shows results similar to those observed in experiments or predicted by finite element models [see *Lebensohn et al.*, 2003]. However, these methods have the limitation that they only simulate viscoplastic deformation and that dynamic recrystallization is only incorporated by using probabilistic models. For instance, *Signorelli and Tommasi* [2015] successfully simulated subgrain rotation recrystallization and the resulting CPOs in olivine with the VPSC approach, but using an ad hoc probabilistic law for grain size reduction. In a similar way, the kinematical code D-REX [*Kaminsky and Ribe*, 2001] incorporates dynamic recrystallization processes through two dimensionless parameters that account for grain boundary migration and nucleation. However, all these methods are not full-field, and therefore cannot model the full range of intracrystalline heterogeneities and intercrystalline interactions that develop in polycrystals. Apart from these disadvantages, all the methods mentioned above do not

allow to visualize the explicit evolution of the microstructures with deformation and are only restricted to the texture, and sometimes grain size evolution.

Full-field models provide a promising alternative approach to model microstructural evolution [*Moulinec and Suquet*, 1995; *Lebensohn*, 2001; *Castelnau et al. 2008; Lebensohn et al.*, 2008; *Amodeo et al. 2016]*. Recently, a full-field crystal viscoplastic approach based on the Fast Fourier Transform (VPFFT) [*Moulinec and Suquet*, 1995; *Lebensohn*, 2001; *Lebensohn et al.*, 2008] has been integrated within the ELLE software platform [*Jessell et al.*, 2001] to simulate coupled geological processes during deformation and metamorphism [*Griera et al.*, 2011; *Griera et al.*, 2013; *Llorens et al.*, 2013a; *Llorens et al.*, 2013b; *Llorens et al.*, 2016a; *Llorens et al.,* 2016b; *Llorens et al.,* 2017; *Steinbach et al.*, 2017]. In this model the laws controlling grain size reduction and intracrystalline recovery are defined from the mapped variation of misorientations related to the relative misfit between local lattice orientations, providing a more realistic framework for the simulation of microstructures. Additionally, this code is able to simulate the spatial evolution of deformation, which has a strong influence on the resulting microstructures, and can model processes such as strain localization up to high strain [*Llorens et al.*, 2016b]. This method allows a full control on the relative contribution of each deformation mechanism during microstructure evolution. Finally, although VPFFT/ELLE is expensive in computational time, it provides results in the same format as those obtained with EBSD analysis from natural and experimental samples, allowing direct comparisons (e.g., *Piazolo et al.*, [2004]).

This contribution presents numerical simulations of pure halite deformation and recrystallization under dry conditions at relatively low temperatures (< 200°C) up to a shear strain of four, with the aim of understanding the behavior of polycrystalline aggregates undergoing subgrain rotation recrystallization. At these temperatures, the rate of grain boundary migration (GBM) is negligible, hence only intracrystalline recovery is considered here. We briefly introduce the VPFFT/ELLE method and present a series of numerical experiments in which a polycrystalline aggregate is deformed varying the strength along halite slip systems. Viscoplastic deformation is coupled with a process that simulates intracrystalline recovery associated with the decrease of free energy by subgrain rotation. In this way, we evaluate the competition between dislocation glide and recovery, and show how the interplay between these processes influences the resulting microstructures. Moreover, we assess the use of subgrain misorientations as a strain gauge in situations of simple shear deformation incorporating dynamic recrystallization by subgrain rotation and recovery. Since most rocks undergo intracrystalline recovery during and after deformation, we aim to understand how this process affects the strain gauge and whether misorientations can also be used to unravel the environmental conditions associated with recovery (i.e., temperature). The numerical results match well those from coaxial experiments by *Pennock et al.* [2005], torsion experiments by *Armann* [2008] or CPO modelling by *Wenk et al.* [2009], and allow the study of microstructures in a wider range of conditions than those in the laboratory. This numerical method is not restricted to halite, but can potentially be expanded in order to incorporate more deformation processes, refined and applied to less studied and less accessible polycrystalline aggregates of minerals with a similar structure and slip systems, such as magnesiowüstite in the lower mantle.

2 Methods

The microstructural evolution of a pure halite polycrystalline aggregate during creep by dislocation glide (in a power-law creep regime) and recrystallization is numerically simulated

using the software platform ELLE [*Jessell et al.*, 2001; http://www.elle.ws]. ELLE is open-source software for the simulation of rock microstructures during deformation and metamorphism. Our models are based on the coupling of a full-field viscoplastic formulation based on the Fast Fourier Transform (VPFFT code; *Lebensohn* [2001]; *Lebensohn et al.* [2008]) and ELLE modules to simulate recovery [*Borthwick et al.*, 2014]. ELLE has been successfully used to model a range of coupled microstructural processes, such as static grain growth, strain localization, dynamic recrystallization, rotation of rigid objects in anisotropic rocks, folding and coupled deformation and recrystallization of polar ice [e.g., *Griera et al.*, 2011; *Griera et al.*, 201*3; Llorens et al., 2013a; Llorens et al., 2013b; Llorens et al.*, 2016a; *Llorens et al.*, 2016b; *Llorens et al.*, 2017; *Steinbach et al.*, 2017, and references thereof]. The last four of these studies made use of the coupled VPFFT/ELLE approach that it is utilized for our simulations. This method allows simulating deformation of a polycrystalline aggregate by dislocation glide and dynamic recrystallization up to high strains, similar to those observed in nature.

The VPFFT code calculates lattice rotations associated with viscoplastic deformation. From these data, recrystallization processes such as grain boundary migration, new grain nucleation or intracrystalline recovery can be simulated using ELLE processes (see descriptions below). In the present study, only the process of recovery is considered, while grain boundary migration, new grain nucleation and grain boundary sliding are deliberately not incorporated. This contribution therefore aims to study the process of subgrain rotation recrystallization in isolation, prior to its coupling with other recrystallization processes in future studies. Our simulations thus cover the idealized regime II (rotational-recrystallization dominated) of *Hirth and Tullis* [1992]. This is coherent with results from pure-halite deformation experiments under dry conditions and relatively low temperatures (lower than 200°C), where the three last processes are not active [*Urai et al.*, 2008]. We therefore concentrate on the analysis of the competition between (i) grain size reduction caused by dislocation glide and (ii) subgrain coarsening by coalescence through rotation and alignment of the lattices of neighboring subgrains (SGC), associated with intracrystalline recovery. The recovery (SGC) process reduces subgrain misorientations associated with the decrease of free energy (i.e., boundary and stored strain energies), thus producing coarsening and coalescence of subgrains that compensate grain size reduction associated with dislocation glide.

2.1 VPFFT – Viscoplastic deformation

In this section we provide a brief summary of the VPFFT approach. A more detailed explanation of the code and how it is implemented can be found in *Lebensohn* [2001] and *Lebensohn et al.* [2008]. This FFT-based code is a full-field formulation that provides a solution of the micromechanical problem by finding a stress and strain-rate field that minimizes the average local work rate under the compatibility and equilibrium constraints (see *Lebensohn* [2001]). In this full-field approach, lattice orientations are mapped on a rectangular grid of Fourier points or unconnected nodes (*unodes*) that represent small material elements and that are also used to store local stress, strain rate and dislocation densities. Lattice rotations due to plastic deformation by dislocation slip are calculated from the velocity gradient and stress fields. The local mechanical response of a non-linear heterogeneous material can be calculated as a convolution integral between Green functions associated with a linear homogenous medium and a polarization field containing all the information on the heterogeneity and nonlinearity of the material's behavior. For periodic media, the Fourier transform allows converting convolution integrals in real space to simple products in the Fourier space. Therefore, the FFTs are used to transform the polarization

field into Fourier space, and thus get the mechanical fields by transforming the convolution product back to real space. Since the polarization depend on the unknown mechanical fields, an iterative method is used to obtain a compatible strain-rate field and a stress field in equilibrium related by the constitutive equation.

The viscoplastic behavior of polycrystals is defined using a non-linear viscous rate-dependent model, where deformation is assumed to be accommodated by dislocation glide [*Lebensohn*, 2001] along a number of pre-defined slip systems. The constitutive equation between the strain rate $\dot{\varepsilon}_{ij}(\mathbf{x})$ and the deviatoric stress $\sigma'(\mathbf{x})$ is given by:

$$\dot{\varepsilon}_{ij}(x) = \sum_{s=1}^{N_s} m_{ij}^s(x)\dot{\gamma}^s(x) = \dot{\gamma}_0 \sum_{s=1}^{N_s} m_{ij}^s(x) \left|\frac{m^s(x):\sigma'(x)}{\tau^s(x)}\right|^q sgn(m^s(x):\sigma'(x)), \quad (1)$$

where m^s, $\dot{\gamma}^s$ and τ^s are the symmetric Schmid tensor, the shear strain rate and the critical resolved shear stress defined for the slip system s, respectively. $\dot{\gamma}_0$ is the reference strain rate, q is the rate sensitivity exponent and N_s is the number of slip systems in the crystal.

Once the iteration converges, the microstructure is updated using an explicit scheme assuming that the mechanical fields are constant during a small time increment Δt. The new position of a point $\mathbf{x}$ of the Fourier grid is determined using the velocity fluctuation term $\tilde{v}_i(\mathbf{x})$ (Eq. 25 in *Lebensohn* [2001]) arising from the heterogeneity field as

$$X_i(\mathbf{x}) = x_i^0 + \left(\dot{E}_{\iota J} x_j^0 + \tilde{v}_i(\mathbf{x})\right) \times \Delta t, \quad (2)$$

where $\dot{E}_{\iota J}$ is the macroscopic strain rate. The local crystallographic orientations are updated according to the following local lattice rotation

$$\omega_{ij}(x) = \left(\dot{\Omega}(x) + \tilde{\omega}(x) - \dot{\omega}_{\iota J}^p(x)\right) \times \Delta t, \quad (3)$$

where $\dot{\Omega}(x)$ is the average rotation rate of the macroscopic velocity gradient tensor, $\tilde{\omega}(x)$ is the local fluctuation in the rotation-rate obtained by taking the antisymmetric part of the velocity gradient fluctuation term $\tilde{v}_{i,j}(\mathbf{x})$, and finally the last term $\dot{\omega}_{\iota J}^p(x)$ is the plastic rotation-rate of the crystal lattice that it is calculated as $\sum_{s=1}^{N_s} \alpha_{ij}^s(x)\dot{\gamma}^s(x)$, where α_{ij}^s is the anti-symmetric Schmid tensor. Lattice misorientations between neighboring Fourier points form where rotation gradients develop, as a consequence of the formation of deformation gradients. As such, high subgrain misorientations develop in areas of high strain gradients. After VPFFT induces lattice rotations, and before the intracrystalline recovery process, a routine checks if the local misorientation exceeds the local misorientation angle that defines a high-angle grain boundary (HAGB). A new HAGB is thus created when misorientation exceeds 15°. This results in the formation of recrystallized, new grains, and hence in grain size reduction. Grains in the model are defined by nodes that are connected by straight grain-boundary segments, and therefore named boundary nodes (*bnodes*). As grain boundary migration [e.g., *Piazolo et al.*, 2002; *Llorens et al.*, 2016a; *Llorens et al.*, 2016b; *Llorens et al.*, 2017] is disabled in this study, the only role of HAGBs is to restrict recovery and subgrain-boundary formation within individual grains. *Bnodes* are displaced by deformation according to Eq. (2).

2.2 ELLE – Intracrystalline recovery

After each deformation step, the new microstructure configuration provided by the VPFFT calculation is used by the ELLE-recovery module that simulates intracrystalline recovery that is driven by a reduction of the local misorientation generated by dislocations, following a modification of the method of *Borthwick et al.* [2014] and *Llorens et al.* [2016a] (see Supporting Information for a full description of the method). Lattice-orientation heterogeneities are reduced by local rotation of the lattice without moving high-angle grain boundaries (HAGB). The recovery routine simulates annihilation of dislocations and their rearrangement into low-angle subgrain boundaries (i.e., polygonization; *Urai et al.* [1986]) and the development of areas with homogenous crystal orientations by coalescence through rotation and alignment of the lattices of neighboring subgrains.

The smallest region with a homogenous lattice orientation in the model is a *unode* (unconnected node), which is treated as a subgrain or crystallite. Geometrical necessary dislocations arise from orientation differences between the lattices in adjacent *unodes*. Rotation of the lattice in one single *unode* changes these orientation differences and, hence, the local dislocation density and associated energy. Since all geometrically necessary dislocations are located at the boundaries between *unodes*, their energy can be treated as a boundary energy that is a function of orientation difference between *unodes*. The recovery routine essentially calculates and applies small increments of lattice orientation in individual *unodes* that is driven by the associated dislocation energy reduction. The model assumes that the rotation rate of a crystallite/subgrain is proportional to the torque (Q) generated by the change of surface energy associated with the misorientation reduction [*Randle*, 1993]. A linear relation between the angular velocity ω and a driving torque Q is assumed

$$\omega = M'Q \qquad (4)$$

where *M'* is the rotational mobility [*Moldovan et al.*, 2002]. Considering a 2D microstructure, the torque acting on a crystallite delimited by *n* subgrain boundaries (*sb*) is given by

$$Q = \sum_n l_{sb}\, d\gamma_{sb}/d\theta_{sb} \qquad (5)$$

where l_{sb} denotes the boundary length with grain boundary energy γ_{sb} and misorientation angle θ_{sb} across the boundary between the reference subgrain and a neighboring subgrain *sb*. In the model, each crystallite (*unode*) is regarded as a small, square (potential) subgrain. For low-angle boundaries, the boundary energy is calculated as a function of the misorientation angle with the Read-Shockley equation [*Read and Shockley*, 1950]. For such misorientation angles, the equivalent rotations by crystal symmetry are considered in order to obtain the minimum misorientation θ between two crystallites or *unodes* (i.e., disorientation). In the original model by *Moldovan et al.* [2001; 2002], the rotation mobility *M'* was expressed as function of boundary and/or lattice self-diffusion. Here, our approach differs from the original one because we have assumed that *unode* (crystallite) lattice rotation is accommodated by cooperative motion/rearrangement of boundary dislocations (*Li* [1962]), by reducing the local misorientation. Since we assume rigid rotation of square *unodes*, a mechanism of boundary and lattice diffusion is required in order to keep areas constant along their edges. Due to the lack of experimental data on rotation mobility, and as a first approach, we assume that subgrain rotation can be described as

a linear viscous process where *M'* is expressed as function of the effective viscosity of the material η (see Supporting Information for the full description). For a square shape this relationship is

$$M' = \frac{1}{8\eta}\frac{1}{d^2} \tag{7}$$

where *d* is the subgrain size (i.e., one *unode*).

The recovery process in ELLE assumes that each *unode* is a potential subgrain and thus the boundary energy and misorientation is minimized by the rotation of each *unode*. The algorithm starts by choosing a random *unode* and finding the first-neighboring *unodes* that belong to the same grain. The crystal orientation of the reference *unode* is rotated towards the value that results in the maximum reduction in energy calculated from systematic trial rotations, being the crystal orientation unchanged if all trial positions result in an increase of energy of the neighborhood. This procedure is repeated for each *unode* in random order every time step. The numerical predictions were verified by *Borthwick et al.* [2014] using results from intracrystalline evolution during annealing experiments of deformed single salt crystals. Our method presents some slight differences with that of *Borthwick et al.* [2014]. These are that: (i) rotation in our approach depends on the boundary energy reduction and (ii) we use a direct relationship between *M'* and the material properties based on the material's effective viscosity (see Supporting Information for more details). An alternative way to constrain *M'* could be based on the use of misorientation decay during annealing experiments. Although there is data from high-temperature halite experiments [e.g., *Borthwick et al.* 2012 and references therein], there is certainly no published data for halite deformed in the low-temperature regime. Therefore, the approach taken is the most appropriate for estimating *M'* values. A comparison of the kinetics of recovery calculated from annealing experiments versus those using our approach is discussed in the Supporting Information and Figure S1.

2.3 Experimental setup and postprocessing

An initial microstructure composed of 255 grains is discretized into a resolution of 256x256 Fourier points (or *unodes*), resulting in a unit cell formed by 65,536 nodes (Figure S2a,b). These nodes provide the physical properties within grains and store the dislocation density and lattice orientation, defined with the three Euler angles. A set of random initial orientations (Figure 1) was assigned to the initial grains, and the initial crystal preferred orientation (CPO) results in near isotropic bulk behavior. The data structure on VPFFT/ELLE is fully periodic, in a way that grains reaching one side of the model continue on the other side. The initial model is a 1x1 cm square and, therefore, the *unode* distance is set to *d*=1/256 cm. Every deformation time step all the parts of the model outside the square unit cell are repositioned back into it (Figure S2c). This improves the visualization of the microstructures, even when high shear strains are reached. In ELLE, each process is simulated as a separate module that acts on the data structure [*Jessell et al.*, 2001]. The program flow and coupling between the viscoplastic VPFFT code and ELLE are similar to those used by *Griera et al.* [2011], *Griera et al.* [2013], *Llorens et al.* [2016a], *Llorens et al.* [2016b], *Llorens et al.* [2017] and *Steinbach et al.* [2017]. Each process is activated sequentially in a loop that represents a small increment $\Delta\gamma$ of viscoplastic deformation calculated with VPFFT followed by recovery during a small time increment Δt. Since an elastic component is not incorporated in our models, the mechanical response of the viscoplastic model only depends on the current

configuration. Moreover, VPFFT assumes that all the slip systems have already reached a yield condition, and therefore the current stress field only depends on the current lattice orientation field. Therefore, the approach of simulating processes sequentially is appropriate for the present models. Additionally, the same operator-splitting procedure of coupling processes sequentially has been successfully used in a number of viscous and viscoplastic numerical simulation studies utilizing the ELLE platform (see *Piazolo et al.* [2002], *Bons et al.*, [2008], *Jessell et al.* [2009], *Griera et al.* [2013], *Llorens et al.* [2013], *Llorens et al.* [2017], *Steinbach et al.* [2016] and references thereof), and tested for our specific model configuration (see below).
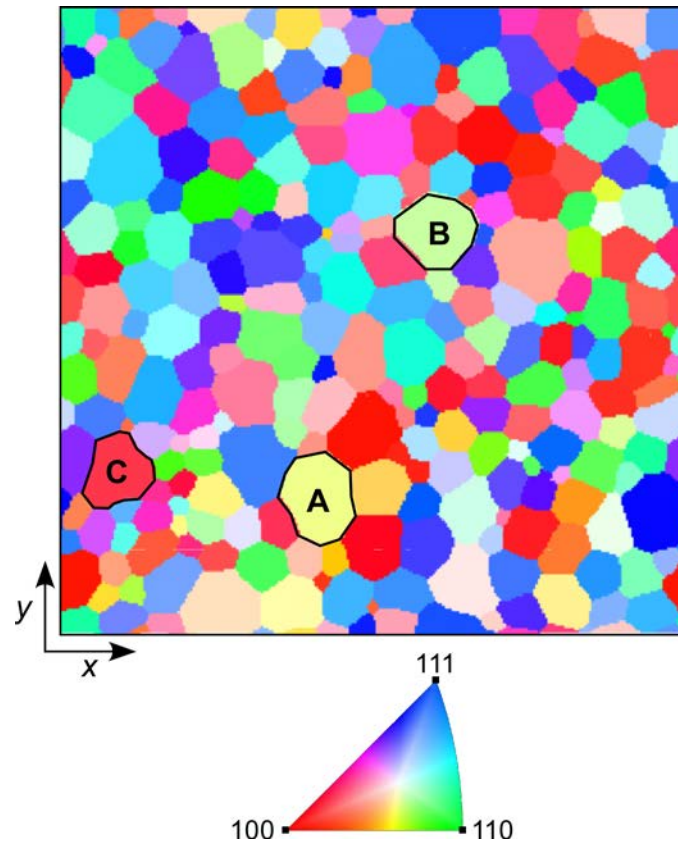
Figure 1. Initial model configuration, with the original orientation of grains. Three grains are selected for a more detailed analysis (shown in Figure 5). Orientations are shown with respect to the *x* axis.

The constitutive behavior of halite polycrystals is simulated using a system with cubic symmetry where deformation is accommodated by three sets of slip systems: $\{110\}\langle\bar{1}10\rangle$, $\{100\}\langle011\rangle$ and $\{111\}\langle\bar{1}10\rangle$ [e.g., *Carter and Heard*, 1970]. In this approach, the resistance of slip systems to glide is defined by a critical resolved shear stress (τ^s). The degree of anisotropy (*A*) is set as the ratio between the critical resolved shear stress with respect to the easiest glide system, which is $\{110\}\langle\bar{1}10\rangle$ for halite at low temperature. We have set CRSS as three times higher for the $\{100\}\langle011\rangle$ slip system (i.e., *A*=3), and two times for the $\{111\}\langle\bar{1}10\rangle$ system (i.e., *A*=2) following *Wenk et al.*, [2009] (who proposed these CRSS values after experimental data by *Carter and Heard* [1970]). The stress exponent is set to *q*=7 for all the experiments. From a mechanical point of view, the VPFFT approach assumes that the CRSS' do not change throughout time (i.e., there is no strain hardening associated with interaction of dislocations), and therefore these *A*

values are kept constant throughout the simulation. Such a constant *A* value is warranted as we separately model recovery that counteracts strain hardening.

Dextral simple-shear deformation was modeled in increments of $\Delta\gamma$=0.04 up to γ=4, although significantly higher shear strains can be achieved at the cost of calculation time. Four different recovery scenarios were modeled by varying the number of computational steps of the recovery (SGC - subgrain coarsening) process per deformation step: SGC0, SGC1, SGC10 and SGC25. A constant time step of $2x10^8$ s (~6 years) was used for all simulations and, therefore, the shear strain rate was $2x10^{-10}$ s^{-1}. There are no experimental data to constrain the rotation mobility *M'* parameter used in the recovery models. The *M'* value was calculated with equation (7), taking a reference viscosity of $5x10^{16}$ Pa·s (model SGC1). This value was determined from flow laws derived from halite experiments for the given strain rate (after *Urai et al.* [2008]), assuming a low temperature (< 50 ºC) and for our strain rate. As the strain rate is constant for all models, an increase of the number of recovery steps per simulation time step implies a proportional reduction of the effective viscosity. We interpret this reduction as associated with a temperature increase that causes a higher activity of recrystallization processes. For the SSG10 and SSG25 simulations the estimated viscosities are $5x10^{15}$ Pa·s and $2x10^{15}$ Pa·s, respectively. This range of calculated values is in agreement with bulk viscosities observed from halite deformation experiments for the aforementioned low temperature conditions [*Urai et al.*, 2008]. For the model without recovery (SGC0), the rotation mobility is assumed to be sufficiently small not to produce microstructure modifications for the time and length scale of our simulations. The viscosity of this model should be at least higher than that of the reference model SGC1.

The numerical results were post-processed using the texture calculation toolbox MTEX (http://mtex.googlecode.com; *Bachmann et al.* [2010], *Mainprice et al.* [2011]). MTEX allows generating maps (i.e., lattice orientation, misorientation boundaries) and analyzing the CPOs in a similar way as for EBSD data of natural or experimental samples, thus allowing a direct comparison of 2D sections.

A series of simulations based on the model SGC10 were analyzed in order to investigate the influence of the time step size on the resulting microstructures. For this purpose, we ran models with incremental shear strains of $\Delta\gamma$=0.008, 0.016, 0.024, 0.032, 0.04, 0.08, 0.12 and 0.16, keeping the same balance of subgrain coarsening with respect to shearing. This means that runs with a larger shear strain increment underwent a higher number of recovery (SGC) steps. The results are summarized in Figure S3 (Supporting Information) and demonstrate that the chosen time step size has a very limited influence on the results. This difference is associated with the fact that relatively high misorientations are reduced in the first step of the SGC process. We chose to run the models with a shear strain increment of Δ_{inc}=0.04 per time step as a compromise between accuracy and simulation time. The difference between this base model and that with very small time steps is very small, with a variation of less than 0.2° of the mean misorientation of the model (Figure S3).

3 Results

Orientation maps resulting from the simulations without recovery (SGC0) show a microstructure with strong grain size reduction and increasing elongation of relict grains (defined by the original grain boundaries) with progressive deformation (Figure 2; Movie ms01 of the SGC0 model in additional supporting information). These processes become extreme at relatively

high shear strains, where only a few large relict grains immersed in a recrystallized matrix are recognizable (e.g., Figure 2d at $\gamma=4$). It is worth noting that the term recrystallized matrix here refers to areas of small grains formed by rotation recrystallization (i.e., by the so called grain refinement process in metallurgical and material science). As expected, the angle between the developing foliation and the shear plane progressively reduces with increasing strain, although at $\gamma=4$ the foliation is still oblique to the shear plane. Relict grains tend to show a shape-preferred orientation oblique to the shear plane and coherent with the imposed dextral shear sense. Deformation is distributed along the polycrystal, and no localization bands in areas with preferred grain size reduction can be distinguished. With increasing shear strain, grain orientations trend towards acquiring {110} orientations parallel to the shear direction (i.e., green tones in Figure 2), while very few grains with {111} parallel to the shear direction (i.e., blue tones in Figure 2) can be found.

Grains deform internally in a different way depending on their initial geometry and orientation and those of their neighbors. For example, at relatively low strains ($\gamma=1$) some grains develop a network of subgrains (Figure 2b), while others have homogeneous crystal orientations or smooth orientation gradients without distinct subgrain boundaries. The first detectable low-angle grain boundaries (LAGB; smaller than 15º) tend to form next to triple nodes, because orientation differences between grains in these areas tend to result in strain incompatibility and therefore lead to the activation of different slip systems. Some of these LAGBs subsequently develop into high-angle grain boundaries (HAGB; higher than 15º) to form new and smaller grains, which display a parent and daughter grain structure between relict and recrystallized grains (i.e., formed by rotation recrystallization). Areas with recrystallized grains tend to be initially isolated, surrounding parental grains. With progressive strain these areas tend to join and form connected bands that finally result in a continuous matrix at higher strain. At relatively low strains ($\gamma=1$) new grains formed by rotation recrystallization tend to be grouped in clusters. Grains with denser subgrain networks have a tendency to have {100} close to the shear direction (red tones in Figure 2). The orientation of subgrain boundaries in banded grains generally varies between the direction of the grain elongation or foliation and the shear plane. Subgrain rotation significantly increases with progressive strain, causing a strong grain size reduction in the SGC0 model.

Simulations that include intracrystalline recovery show that subgrain coarsening and coalescence significantly reduce subgrain misorientations and therefore the density of subgrain boundaries. Thus, the intensity of grain size reduction is significantly lower in those models, allowing the survival of larger grains and subgrains with progressive deformation (Figure 3; Movie ms02 of the SGC0 model in additional supporting information). Crystal preferred orientations (CPOs) are qualitatively not changed when there is recovery, but their intensity is
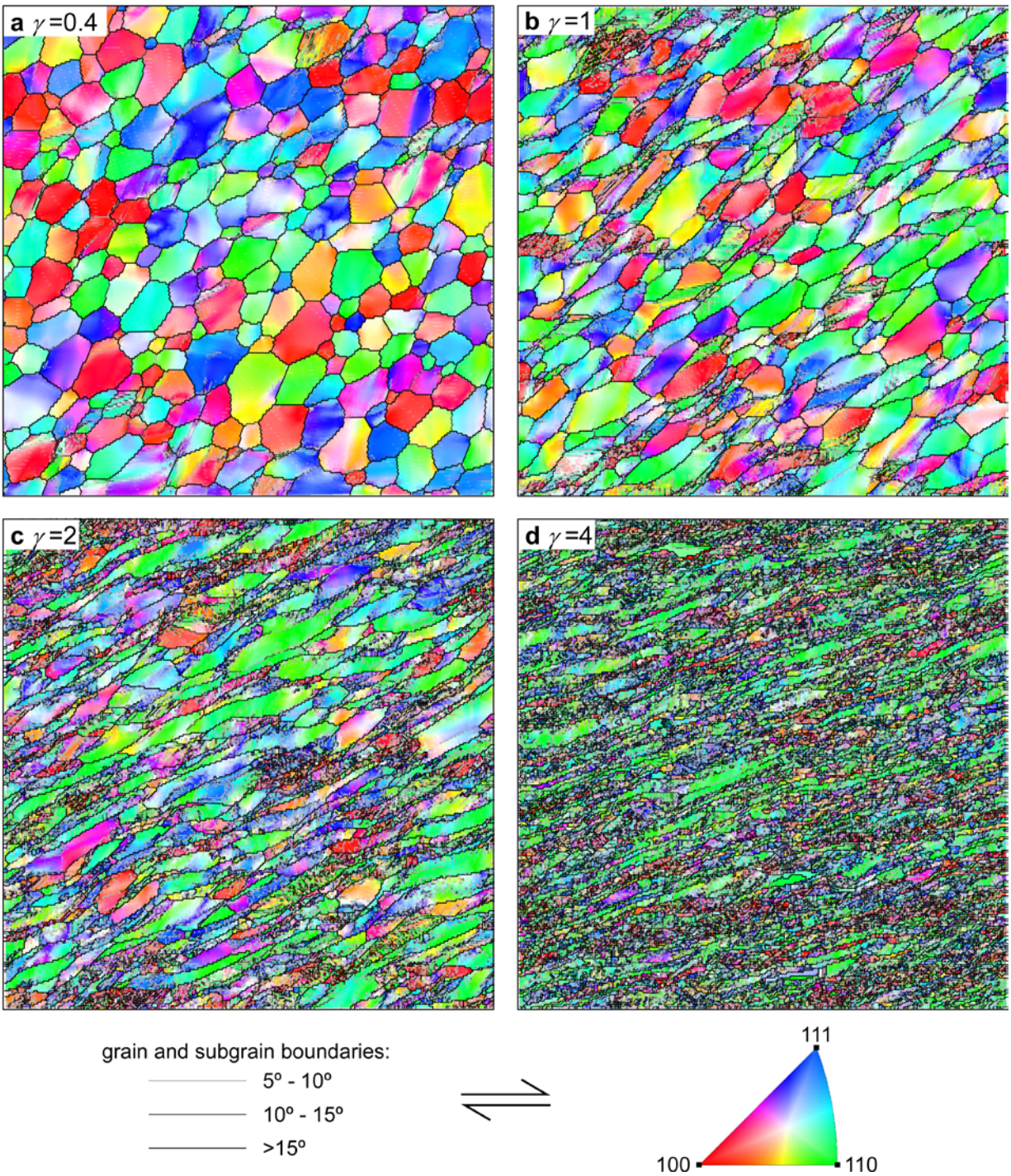
Figure 2. Orientation and grain boundary map of a simulation SGC0 with only viscoplastic deformation, i.e., without recovery (SGC0). Orientations are shown with respect to the horizontal *x* axis. The trace of the shear plane is horizontal and the shear sense is dextral in this and the following figures.
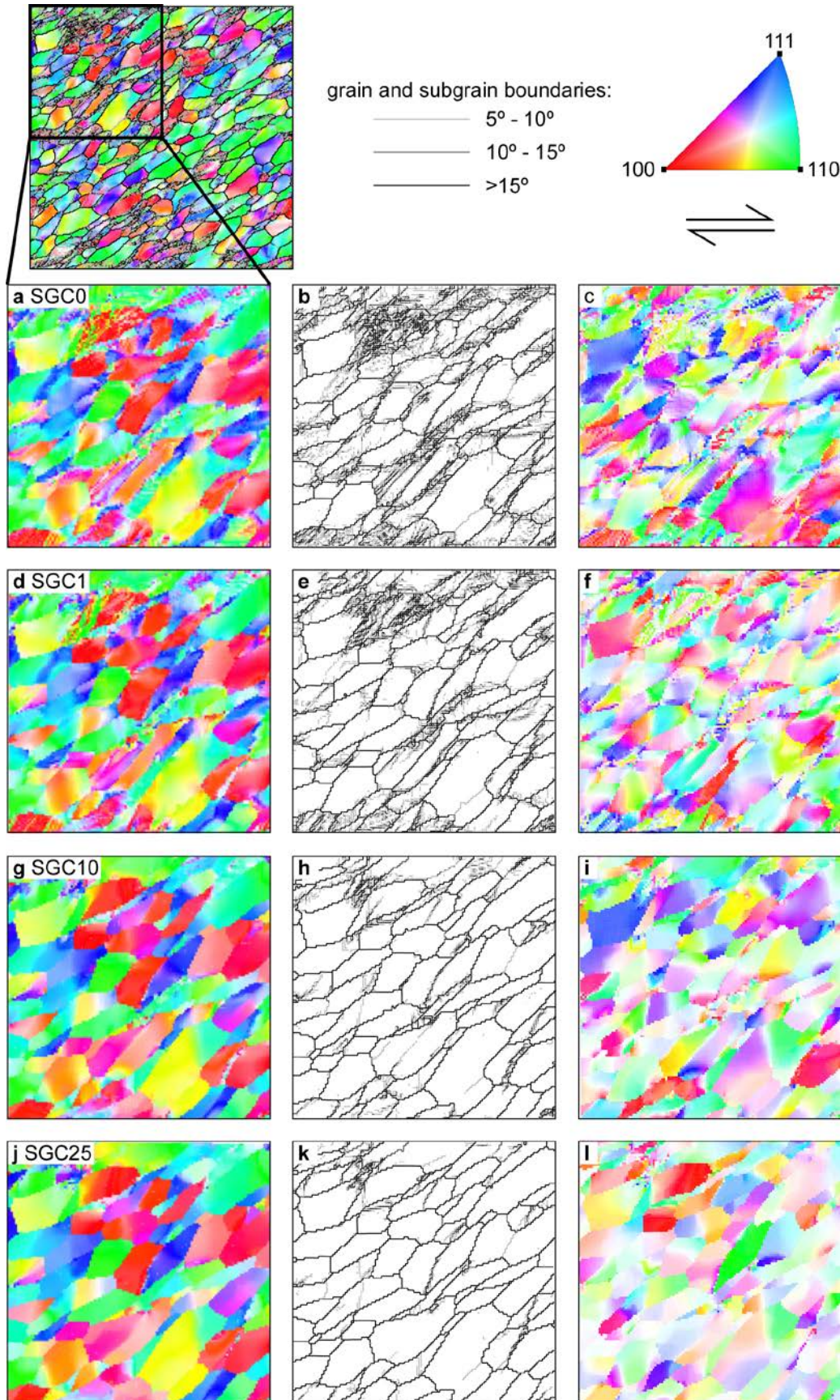
Figure 3. Orientation and grain boundary map of a series of simulations with different degrees of recovery, at a shear strain of $\gamma=1$: (a-c) SGC0 (no recovery, only viscoplastic deformation), (d-f) SGC1, (g-i), SGC10, (j-l), SGC25 (1, 10 and 25 steps of recovery per deformation step, respectively). (a), (d), (g) and (j) show EBSD crystal orientation maps (as in Figure 2). (b), (e), (h) and (k) display misorientation maps. (c), (f), (i) and (l) show the misorientation with respect to the mean of the grain, using the original grains as reference (Figure 1). Note that in order to show details only one fourth of the model area is displayed.

enhanced (Figures 3 and 4). Subgrain-free grains dominate in simulations with strong recovery (SGC10 or SGC25; Figure 3g-l), with many grains having internal misorientations lower than 5°. Orientation maps of the deviation of individual *unodes* or crystallites with respect to the mean orientation of the grain help to highlight the subgrain structure (Figure 3c,f,i,l). Strong subgrain size reduction with significant deviations from the mean orientation of the grains can be seen in simulations with low or no recovery (SGC1 or SGC0). However, increasing recovery strongly reduces these deviations and the map shows clearer (white) areas, meaning that the misorientation of crystallites with respect to the grain mean is very low.

A close look at the grains better reveals the effects of recovery. For example, Figure 5 shows details of three selected grains (indicated in Figure 1), comparing the experiment without recovery (SGC0) with that with 10 steps of recovery per deformation step (SGC10). The increase of recovery reduces the spread of orientations and decreases subgrain boundary misorientations. The results illustrate how two grains with relatively similar initial orientations (A and B) develop different lattice orientation distributions after a shear strain of one. Three subgrains with very different orientations develop in grain A. The new grain limits are subparallel to the shear plane. Contrary to this, grain B develops banded subgrains, with alternating orientations. The new grain boundaries within this grain are oriented parallel to its elongation direction. Grain C shows the same orientations in both cases, although there are more subgrain boundaries in the model without recovery (SGC0). For the three cases, subgrain boundaries are sub-parallel to a direction of the {110} planes. There is a maximum clustering of axes parallel to the <100> direction (i.e., parallel to the normal of the intermediate strain axis of simple shear deformation). On the contrary, the other axes are more dispersed. This indicates that the misorientation axes for this type of boundaries is <100> and corresponds to a tilted boundary, as this axis is included in the boundary plane.

Pole figures reveal that crystal orientation poles are oriented almost identical for the whole series of experiments, but there is more scattering and a less intense CPO in the models with limited or no recovery. At all stages of deformation, orientations are spread, as indicated by orientation maps (Figures 2 and 3) and pole figures (Figure 4). Despite the scattered distribution, the {110} and {111} pole figures at $\gamma=1$ already display a weak hexagonal symmetry, both in models with and without recovery. On the contrary, the {100} stereogram shows a more asymmetric pattern, which evolves with progressive deformation towards a pattern with a maximum perpendicular to the shear plane and two maxima at 45° to it. At $\gamma=4$ there are two {110} maxima parallel to the shear plane, plus another four maxima at 45° of it. Four {111} maxima form at 45° to the shear direction. Lattice orientation of crystallites in individual grains display some scatter, but show a similar symmetry to that of the bulk CPO (Figure 5). However, they can appear rotated depending on the initial orientation of the selected grain and its neighbors.
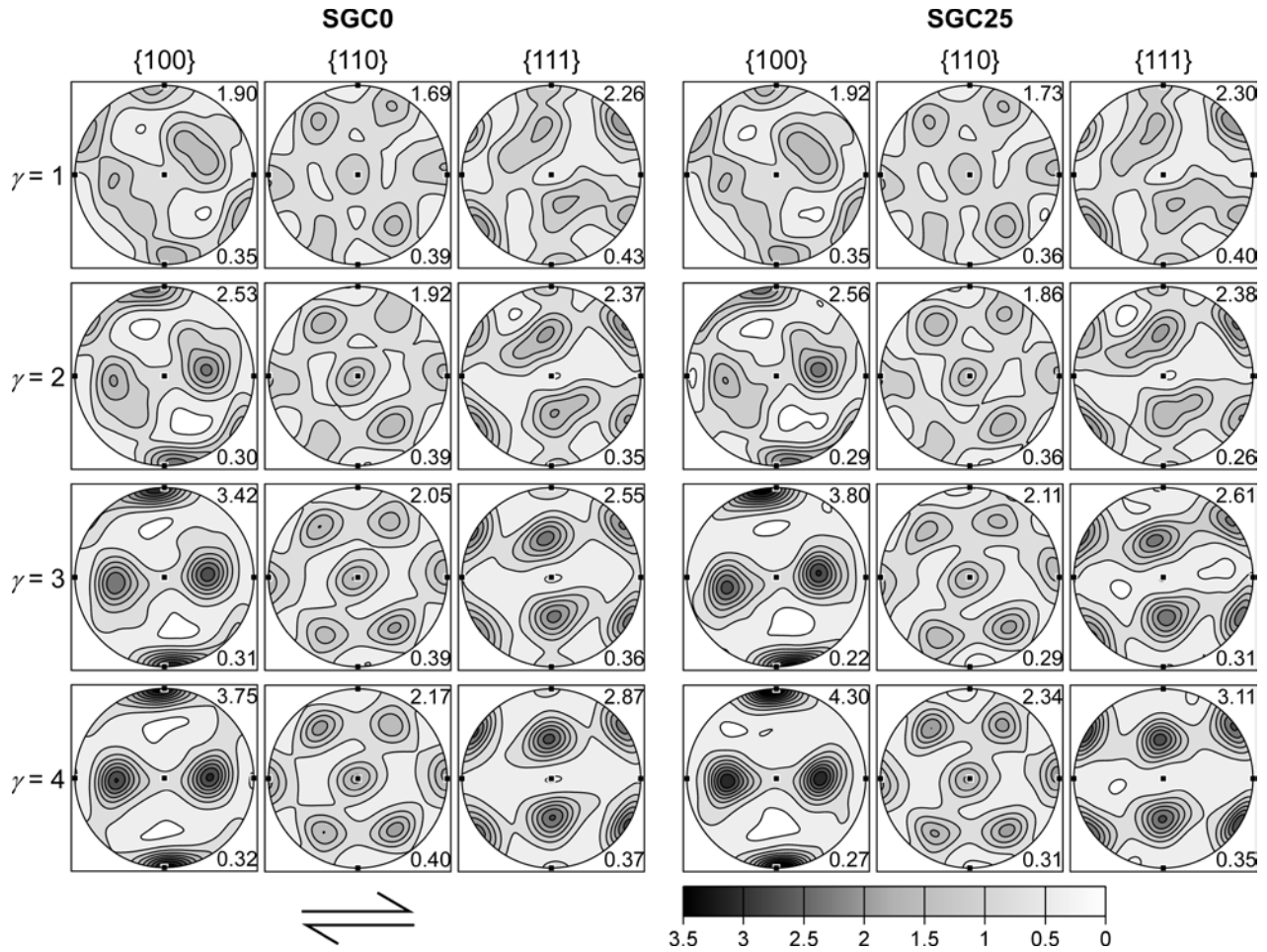
Figure 4. Pole figures for the simulations shown in Figure 3. Stereograms on the left and right groups of columns show the CPO evolution for the simulations without recovery (SGC0) and with 25 steps of recover per deformation time step (SGC25), respectively. Equal area projection, with linear contour intervals. The pole figures show that the addition of the recovery process has remarkably little effect on the CPO's.

The analysis of the slip system activity reveals that the three sets of pre-defined slip systems all contribute to deformation (Figures 6 and 7). In all our simulations, nearly 50% of strain is accommodated, on average, by the {111} systems. At the onset of deformation, when grain distribution is random, 48% of strain is accommodated by these systems, 34% by the easiest glide {110} system, and 18% by the hardest {100} systems. In order to check the consistency of these values, the SGC0 simulation was repeated ten times with different initial grain orientations, and the maximum deviation of bulk activities at $\gamma=1$ was ±0.4%. With increasing strain, the activity of {111} systems remains approximately constant, while that of the {110} system slightly decreases and {100} increases. At $\gamma=4$, and for the model without subgrain coarsening, 29% of strain is accommodated by the {110} system and 24% by {100}. When there is recovery, the activity of {111} system remains similar but the activity balance between the hardest and easiest slip systems slightly changes throughout the experiment, although the activity of the {110} system is always higher than that of the {100} (Figure 6d at $\gamma=4$). Maps displaying the distribution of slip system activity show that the {111} systems dominate and widely affect the whole sample (blue tones in Figure 7). The relative activity of the second slip system, either {110} (green) or {100} (red), determines the evolution of each grain and results in stress
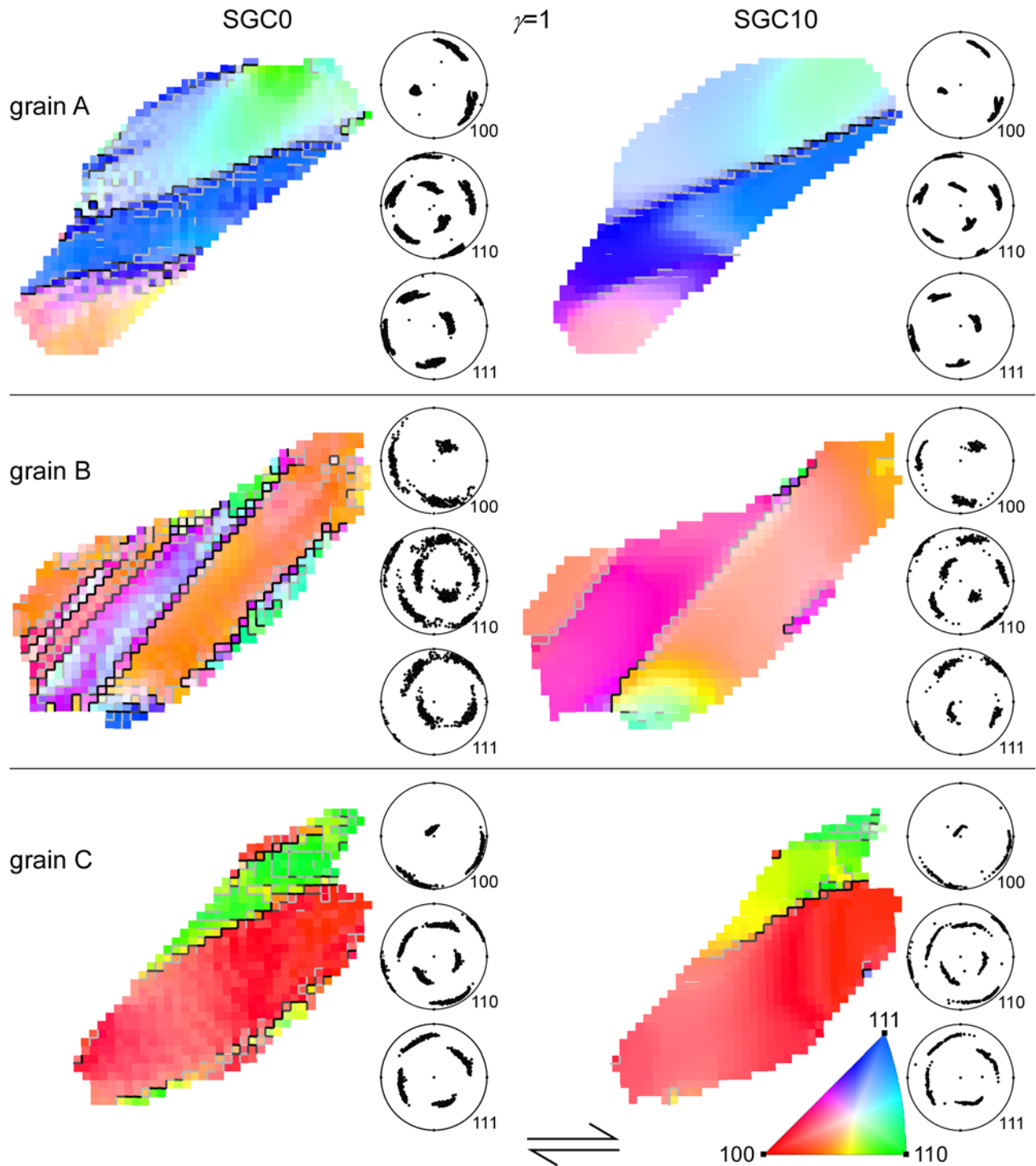
Figure 5. Orientation and grain boundary maps showing details of three selected grains (see Figure 1 for their original orientation and geometry) in the models with SGC0 and SGC10 at γ=1.The addition of subgrain coalescence reduces subgrain boundary misorientations and reduces the crystal orientation spread and the formation of grain and subgrain boundaries. Note that the color coding for grain boundaries is the same as in Figures 2 and 3.
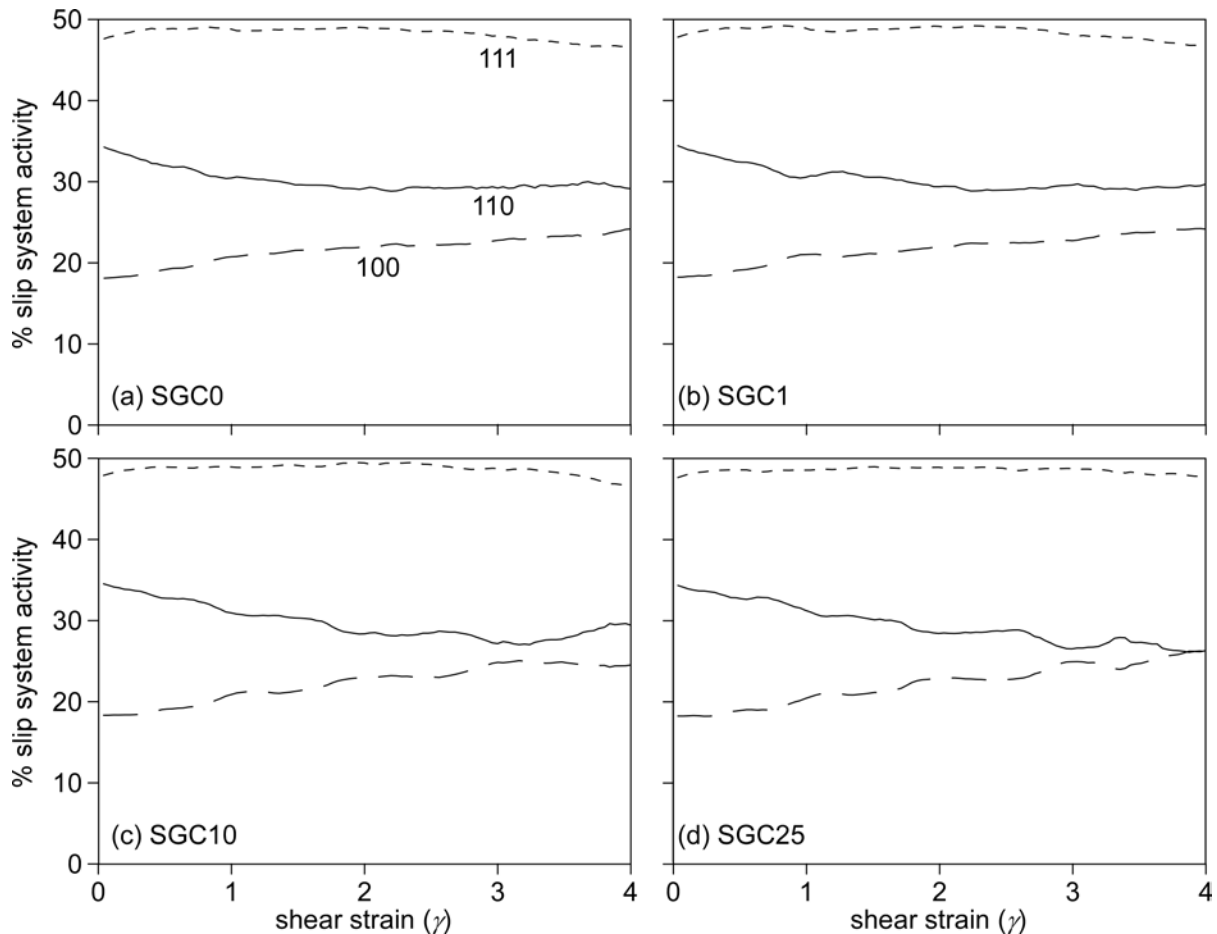
Figure 6. Evolution with progressive strain of the slip system activity for the different simulations, calculated as the average of all *unodes* or crystallites in the simulation.
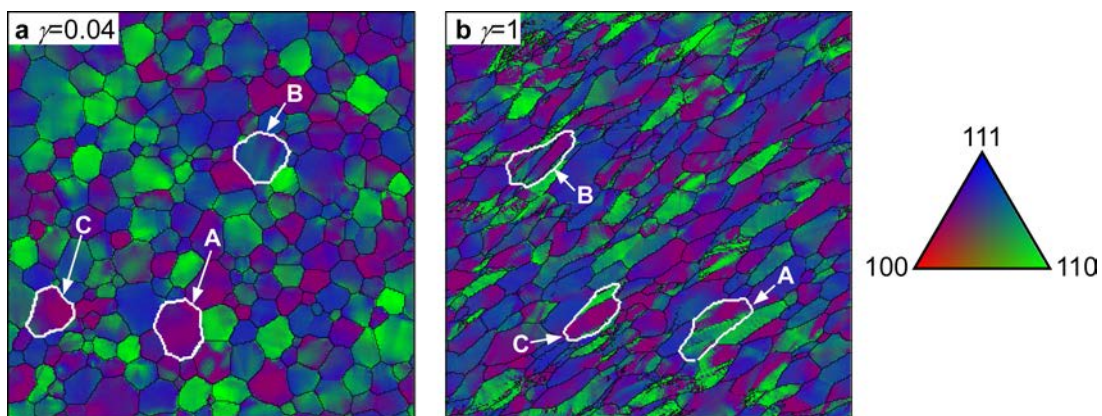

Figure 7. Distribution of the slip system activity for the SGC0 simulation, at two deformation stages: (a) γ=0.04 and (b) γ=1.

concentration differences (Figure S4, see supplementary information). Some grains, such as those marked with A, B and C, start displaying banded regions with differences in slip system activity from the onset of deformation (Figure 7a), thus giving rise to subgrains that evolve to form new grains with increasing strain. In some cases, subgrains can form even if the same slip systems

dominate, but they have different activities. The subgrains developed in the lower part of grain A, which are all determined by {110} systems, are a good example of this phenomenon (Figures 5 and 7b). The slip system activity maps are relatively similar in models with and without recovery. For the three selected grains of Figure 5, subgrain boundaries are formed as consequence of differences in the activation of the {110} and {100} sets between subgrains.

The frequency distribution of geometric mean misorientations of initial individual grains is shown in Figure 8. At the onset of deformation, subgrain boundaries showed low mean misorientations, which rapidly increased and spread with progressive deformation. However, the rate of this increase slows down at relatively high strains. The distribution of mean values for individual grains is close to exponential at the beginning of deformation, but becomes closer to normal at higher strains (e.g., at γ=2-4) for the models without recovery (SGC0). When subgrain coarsening is active (in models with SGC>0), mean misorientation values are significantly lower, although their spread is similar to the cases without SGC. Values at higher strains tend to deviate from a normal distribution with increasing SGC.
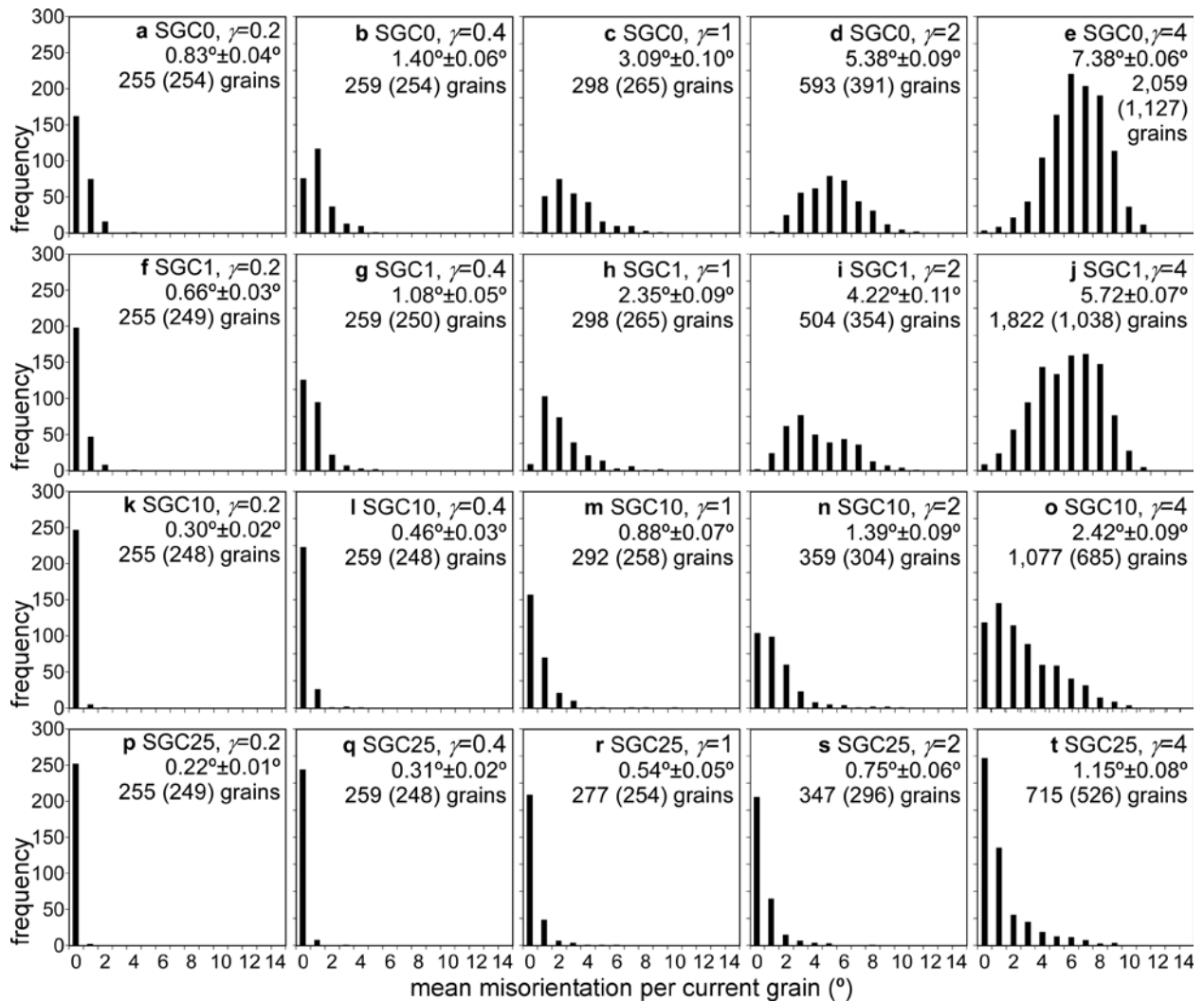

Figure 8. Frequency distribution of grain geometric mean misorientations for different deformation stages (expressed in terms of shear strain γ), for all the experiments performed. Geometric means of misorientation distributions θ_{mean}-

grains are indicated, together with the standard deviation of the mean. Misorientations were calculated with respect to the grains at the current time step, considering that grains form when the misorientation is higher than 15º. The total number of grains is also displayed as an indication of the intensity of grain size reduction. The value in parentheses corresponds to the number of grains that contain at least ten crystallites, and which are considered for the strain gauge discussed in section 4 (see below).

4 Discussion

The main objectives of this study are (i) to investigate the microstructural evolution of halite polycrystals during simple shear deformation with subgrain rotation recrystallization, and (ii) to assess the use of subgrain misorientations as a strain gauge in polycrystals that undergo different intensities of intracrystalline recovery. We specifically simulate halite deformation and recrystallization under dry conditions and at relatively low temperatures, focusing on the competition between (i) grain size reduction by subgrain rotation induced by dislocation glide and (ii) subgrain coarsening driven by the reduction of local misorientation associated with intracrystalline recovery. Our simple-shear simulations produce qualitatively similar results to those from halite deformation experiments by other authors, validating the proposed numerical approach for the simulated deformation regime. Specifically, our numerical microstructures (Figures 2, 3 and 5) and CPOs (Figure 4) can be directly compared with the published torsion experiments of dry halite at 100 and 200 °C by *Armann* [2008] and *Wenk et al.* [2009]. Moreover, they are also in agreement with microstructures of torsion experiments by *Marques et al.* [2013]. Our calculated values of mean misorientation and subgrain misorientation statistics are qualitatively similar to those obtained with EBSD by *Pennock et al.* [2005] for dry halite deformed in coaxial conditions at 165±10ºC.

The experiment without recovery (SGC0) very well illustrates the process of grain size reduction, with the formation of LAGBs that evolve to HAGBs. Subgrains start forming at the early stages of deformation, as in other materials [e.g., *Hurley and Humphreys*, 2003]. Subgrain formation and the development of subgrain misorientations do not only depend on the initial grain orientation, but also on the relative orientations of the surrounding grains. This was also observed in experiments by *Pennock et al.* [2005]. The SGC0 simulation reproduces very similar CPOs as those with the VPSC approach [e.g., *Wenk et al.*, 2009], in which only deformation by dislocation glide is taken into account. In this situation, there is a strong grain size reduction (see evolution of number of grains in Fig. 8a-e), but there are a few relict grains that can survive throughout deformation, depending on their initial orientation and that of their neighbors. As expected, grain elongation increases and rotates towards the shear plane with increasing strain. Orientation maps show a wide distribution, although grains with {110} orientations parallel to the shear direction dominate. The predicted CPOs also reproduce those from low-temperature halite experiments by *Armann* [2008] and *Wenk et al.* [2009] well, although our simulations produce less scattering. This is probably due to the complete absence of other recrystallization processes or deformation mechanisms in the simulations. The addition of recovery changes the deformational behavior of the samples, since subgrain recrystallization associated with the reduction of stored strain and boundary energies significantly decreases grain size reduction (values displayed in Fig. 8), especially in the experiments SGC10 and SGC25. This process does not change CPOs, but results in a more homogeneous microstructure. As indicated in section 2.3, the increase of recovery is simulated with the assumption of a reduction of the effective viscosity of the material, allowing more rotation at the same driving force. Since viscosity is temperature-dependent, this effect would be linked to a temperature increment in natural cases [*Borthwick and Piazolo*, 2010].

A detailed analysis of the slip system activity reveals that the three sets of slip systems all contribute to accommodation of strain, with the {111} systems the most active through time in all numerical experiments. This result is consistent with the VPSC simulations of *Wenk et al.* [2009] after their models reached a relatively stable slip system activity (at $\gamma \sim 3.5$). This predominance can be explained because there are twelve {111} slip systems, and only six of the other two sets ({110} and {100}). Contrarily to VPSC models, the weakest {110} slip systems dominate over the hardest {100} ones in our simulations. However, this difference varies with progressive strain and is not very marked (Figure 6). Moreover, our results show how subgrain coarsening associated with recovery can also slightly modify the distribution of slip system activity, in addition to non-coaxial flow, making the use of texture patterns to determine slip system activity more complex in such systems. Maps of slip system activity and stress concentrations support this observation (Figures 7 and S4, respectively).
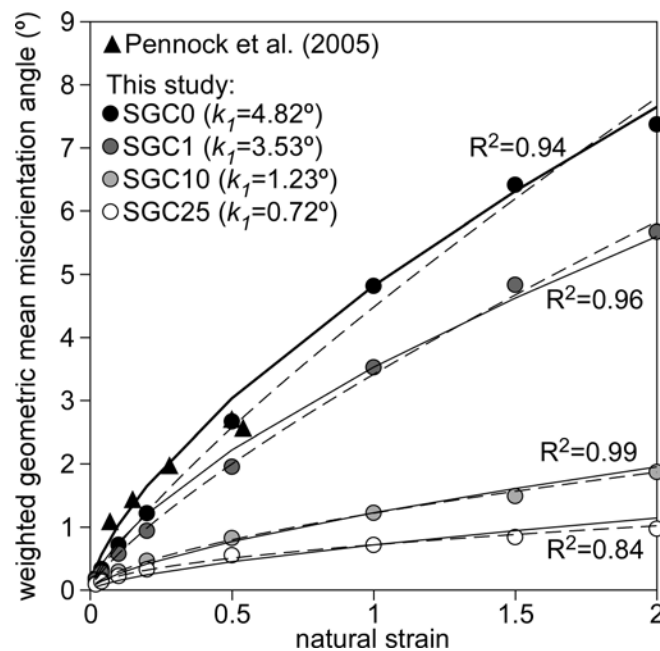

Figure 9. Weighted geometric mean of grain misorientation as a function of natural strain, calculated with equation (8). Geometric means are weighted according to the number of crystallites per grain. Only grains with a minimum of ten crystallites are considered for the calculation. Solid lines show the theoretical power-law relationship for experiments with different intensity of intracrystalline recovery using the k_1 values listed in the legend and a universal n exponent of 2/3 (see discussion section). The R^2 coefficients are calculated with respect to this scaling law. Dashed lines show the best fit for each model (with R^2), with exponents of 0.81 (SGC0), 0.76 (SGC1), 0.66 (SGC10) and 0.53 (SG25). The experimental data from *Pennock et al.* [2005] are displayed and used to calculate the power-law relationship for the experiment without recovery (SGC0) (thick solid line). These data are used as a reference to normalize the results of our series of numerical simulations, at $\varepsilon=1$.

In principle, subgrain misorientations can be used as a strain gauge for dislocation creep deformation in crystalline materials, if we can determine how the misorientation angles correlate with strain [e.g., *Pennock et al.*, 2004; 2005]. This tool can be especially useful for structural analysis in areas where there is a recognizable strain gradient. Over the past 15 years, EBSD mapping has allowed the collection of large misorientation datasets in materials such as metals or halite [e.g., *Randle and Enger*, 2000; *Humphreys*, 2001; *Pennock et al.*, 2002; 2005; 2006; *Hurley and Humphreys*, 2003; *Pennock and Drury*, 2005, among others]. As discussed in the introduction,

a power law relationship of the average subgrain boundary misorientation of the whole sample (θ_{av}) and natural strain (ε) can be found, and this scaling relationship seems to be universal [e.g., *Hughes et al.*, 1997; 1998; 2003; *Pantleon*, 1997; 1998; 2001; *Sethna and Coffman*, 2003]. These studies propose that $\theta_{av} \sim \varepsilon^{n=2/3}$ for geometrically necessary boundaries (GBN's).

    Pennock and Drury [2005] measured $n=0.41$ in halite pure shear experiments, while *Pennock et al.* [2005] obtained $n=0.42$ when using the average subgrain misorientations within grains ($\theta_{av,grains}$), instead of the whole sample:

$$\theta_{av\text{-}grains} = k_1 \, \varepsilon^n \tag{8}$$

where k_1 is a constant, with a value of 3.3° for their experiments. Our subgrain-misorientation data measured on a grain basis closely follow the universal exponent of $n=2/3$ (Figure 9). Note that here we use the geometric mean instead of the average, since this is a more appropriate parameter given that misorientations distributions are frequently non-Gaussian (Figure 8). Moreover, we prefer to calculate a weighted geometric mean, in a way that the contribution of each grain to the mean depends on their number of crystallites. We find that the k_1 constant depends on the intensity of recovery (SGC), and hence on temperature, and k_1 decreases from 4.82° for SGC0 to 0.72° for SGC25 (see list of values in Figure 9). Since only the models with recovery can be scaled, k_1 appears capped at about 4.82° for the model SGC0. The applicability of this law is limited at the other end of the range by the rate where grain boundary migration becomes a significant factor for the subgrain structure. It is important to note that the scaling law is not the best power law fit of the simulation data (Figure 9). With increasing recovery, the best fit exponent decreases from $n=0.81$ for SGC0 to 0.53 for SGC25. However, the coefficients of determination R^2 between these data and the predicted values are high (Figure 9), and therefore the proposed law provides a good approximation. Our results demonstrate that recovery influences the exponent of the scaling law and can help to interpret the low n values obtained by *Pennock and Drury* [2005; 2006] ($n=0.41$-0.42). This low exponent can be related to the activation of intracrystalline recrystallization processes during those deformation experiments, leading to a decrease of intracrystalline heterogeneities and a reduction of n. Our simulations show how the mean subgrain misorientations within grains can be used as a strain gauge in materials undergoing intracrystalline recovery, not only in coaxial deformation conditions but also in simple shear up to high strain. The values obtained confirm that the universal exponent proposed above applies to halite, at least when it is deformed in the absence of grain boundary migration. Additionally, this strain gauge could be potentially applied to rocks that underwent grain boundary migration if grain nuclei keep relatively high misorientations (e.g., as in *Schléder and Urai* [2007]). However, a whole new study would be required to verify this. Unfortunately, our misorientation data cannot be compared directly with those from torsion (simple shear) halite experiments, since *Armann* [2008], *Wenk et al.* [2009] and *Marques et al.* [2013] did not quantify misorientation. Therefore, the strain gauge discussed here does not provide absolute values that can be directly applied to all natural case studies, because further benchmarking against experimental data is required for proper calibration. Additionally, the models presented here only apply to the case of pure dry halite deformed at low temperature, and assume that all deformation is accommodated by dislocation glide with subgrain rotation recrystallization. The values of this strain gauge may change if other mechanisms such as grain boundary migration or grain boundary sliding are active.

The models presented in this contribution reproduce the behavior of dry halite deformed at low temperatures (<200 °C) well. This type of simulation approach may not only be a key to understanding halite rheology, but also that of other minerals with similar symmetry and slip systems. For example, magnesiowüstite deforms plastically in the lower mantle, where it is one of the two major phases, potentially resulting in strain weakening and localized deformation [*Girard et al.*, 2016]. Full-field simulations, such as the ones presented here, can provide new insights into the interplay of deformation mechanisms and resulting flow laws in crustal and mantle rocks, thus improving our understanding of Earth's dynamics. However, further developments are required in order to incorporate additional deformation processes, such as grain boundary migration, grain boundary sliding, new grain nucleation, diffusion processes and hardening of slip systems, among others. Additionally, experimental datasets are needed in order to calibrate numerical models. The simulations presented here are the necessary first step towards a comprehensive full-field model that can account for the deformation of polycrystalline halite and other rocks.

5 Conclusions

We presented a new method to model subgrain rotation recrystallization in polycrystalline aggregates, and applied it to dry halite. The analysis of the resulting microstructures led to the following main conclusions:

- The VPFFT/ELLE numerical approach presented in this contribution accurately reproduces experimental microstructures, allowing the systematic analysis of systems in which multiple deformation processes are active. This full-field method has been applied to halite for first time, providing new insights into the competition between (i) grain size reduction by dislocation glide and (ii) subgrain coarsening by coalescence through rotation and alignment of the lattices of neighboring subgrains, associated with intracrystalline recovery.

- Viscoplastic deformation results in the development of low-angle grain boundaries that evolve to form high-angle grain boundaries, leading to a strong grain size reduction. The activation of subgrain coarsening associated with the decrease of strain stored energy by recovery significantly decreases grain size reduction, although grain orientations are similar in all cases.

- Subgrain coarsening does not significantly modify crystal preferred orientations, but results in less scattered crystal orientations.

- All the sets of pre-defined slip systems contribute to deformation, with changes in their relative activity depending on progressive strain and the amount of subgrain coarsening. These results are in accordance with published laboratory experiments and viscoplastic self-consistent simulations.

- Mean subgrain misorientations per grain can be used as a strain gauge in systems with different degrees of subgrain rotation recrystallization, with a universal scaling exponent of $n \sim 2/3$ that accounts for all cases. The intensity of intracrystalline recovery, and hence temperature, can potentially be estimated with this strain gauge if misorientations can be measured in an area with a strain gradient. This type of strain gauge can be further

developed, refined and calibrated for different geological materials if misorientation data from experiments and field studies are available for comparison with simulations.

Acknowledgments and Data

References

Armann, M. (2008), Microstructural and textural development in synthetic rocksalt deformed in torsion. PhD Thesis, ETH-Zürich, Switzerland.

Ashby, M. F. (1970), The deformation of plastically non-homogeneous materials. Philos. Mag. 21, 399-424.

Bachmann, F., R. Hielscher, and H. Schaeben (2010), Texture analysis with MTEX - free and open source software toolbox. Solid State Phenom. 160, 63-68.

Bons, P.D., D., Koehn, M.W. Jessell (Eds.), (2008), Microdynamic Simulation. Lecture Notes in Earth Sciences 106, Springer, Berlin, 405 pp.

Borthwick, V. E., and S. Piazolo (2010), Complex temperature dependent behaviour revealed by in-situ heating experiments on single crystals of deformed halite: New ways to recognize and evaluate annealing in geological materials. J. Struct. Geol. 32, 982-996.

Borthwick, V.E., S. Piazolo, S. Schmidt, C. Gundlach, A. Griera, P.D. Bons, and M.W. Jessell (2012), The application of in situ 3D X-ray diffraction in annealing experiments: first interpretation of substructure development in deformed NaCl. Mater. Sci. Forum 715-716: 461-466.

Borthwick, V. E., S. Piazolo, L. Evans, A. Griera, and P. D. Bons (2014), What happens to deformed rocks after deformation? A refined model for recovery based on numerical simulations. Geol. Soc. London Spec. Publ. 394(1), 215-534.

Bourcier, M., M. Bornert, A. Dimanov, E. Héripré, and J. L. Raphanel (2013), Multiscale experimental investigation of crystal plasticity and grain boundary sliding in synthetic halite using digital image correlation. J. Geophys. Res. 188, 511-526.

Bunge, H. J. (1985), Representation of preferred orientations. In: Weiss, L. E., Wenk, H. R. (Eds.), Preferred orientation in deformed metals: an introduction to modern texture analysis. Academic Press, London, 73-104.

Carter, N. L., and H. C. Heard (1970), Temperature and rate dependent deformation of halite. Am. J. Sci. 269, 193-249.

Carter, N. L., F. D. Hansen, and P. E. Senseny (1982), Stress Magnitudes in Natural Rock Salt. J. Geophys. Res. 87, 9289-9300.

Erb, U., and H. Gleiter (1979), The effect of temperature on the energy and structure of grain boundaries. Scripta Metall. 13, 61-64.

Farla, R. J. M., H. Kokkonen, J. D. Fitz Gerald, A. Barnhoorn, U. H. Faul and I. Jackson (2010), Dislocation recovery in fine-grained polycrystalline olivine. Phys Chem Minerals, DOI 10.1007/s00269-010-0410-3.

Girard, J., G. Amulele, R. Farla, A. Mohiuddin, and S. Karato (2016), Shear deformation of bridgmanite and magnesiowüstite aggregates at lower mantle conditions. Science 351(6269):144-7.

Griera, A., P. D. Bons, M. W. Jessell, R. Lebensohn, L. Evans, and E. Gomez-Rivas (2011), Strain localization and porphyroclast rotation. Geology 39, 275-278.

Griera, A., M. -G. Llorens, E. Gomez-Rivas, P. D. Bons, M. W. Jessell, L. A. Evans, and R. Lebensohn (2013), Numerical modelling of porphyroclast and porphyroblast rotation in anisotropic rocks. Tectonophysics 587, 4-29.

Guillope, M., and J. P. Poirier (1979), Dynamic recrystallization during creep of single-crystalline halite: an experimental study. J. Geophys. Res. 84, 5557-5567.

Halfpenny, A., D. J. Prior, and J. Wheeler (2006), Analysis of dynamic recrystallization and nucleation in a quartzite mylonite. Tectonophysics 427, 3-14.

Hirth, G., and J. Tullis (1992), Dislocation creep regimes in quartz aggregates. J. Struct. Geol 14, 145-159.

Hughes, D. A., Q. Liu, D. C. Chrzan, and N. Hansen (1997), Scaling of microstructural parameters: misorientations of deformation induced boundaries. Acta Mater. 45, 105-112.

Hughes, D. A., D. C. Chrzan, Q. Liu, and N. Hansen (1998), Scaling of misorientation angle distributions. Phys. Rev. Lett. 81, 4664.

Hughes, D. A., N. Hansen, and D. J. Bammann (2003), Geometrically necessary boundaries, incidental dislocation boundaries and geometrically necessary dislocations. Scr. Mater. 48, 147-153.

Humphreys, F. J. (2001), Review: grain and sub-grain characterization by electron backscatter diffraction. J. Mater. Sci. 36, 3833-3854.

Humphreys, F. J., and M. Hatherly (2004), Recrystallization and Related Annealing Phenomena,. Third ed. Elsevier Ltd, Oxford.

Hurley, P. J., and F.J. Humphreys (2003), The application of EBSD to the study of substructural development in a cold rolled single-phase aluminium alloy. Acta Mater. 51, 1087-1102.

Jessell, M.W., P.D. Bons, L. Evans, T. Barr and K. Stüwe (2001), Elle: a micro-process approach to the simulation of microstructures. Comput. Geosci. 27, 17-30.

Jessell, M. W., P. D. Bons, A. Griera, L. A. Evans, and C. J. L. Wilson (2009), A tale of two viscosities. J. Struct. Geol. 31, 719-736.

Kaminski, E., and N. M. Ribe (2001), A kinematic model for recrystallization and texture development in olivine polycrystals. Earth Planet. Sci. Lett. 189, 253-267.

Karato, S. (2012), Deformation of Earth Materials: An Introduction to the Rheology of Solid Earth. Cambridge University Press. 482 pp.

Kuhlmann-Wilsdorf, D., and N. Hansen (1991), Geometrically necessary, incidental and subgrain boundaries. Scr. Mater. 25(7), 1557-1562.

Lebensohn, R.A. (2001), N-site modelling of a 3D viscoplastic polycrystal using fast Fourier transform. Acta Mater. 49(14), 2723-2737.

Lebensohn, R. A., P. R. Dawson, H. -R. Wenk, and H. M. Kern (2003), Heterogeneous deformation and texture development in halite polycrystals: comparison of different modeling approaches and experimental data. Tectonophysics 370, 287-311.

Lebensohn, R. A., R. Brenner, O. Castelnau, and A. D. Rollett (2008), Orientation image-based micromechanical modelling of subgrain texture evolution in polycrystalline copper. Acta Mater. 56(15), 3914-3926.

Li, J. C. M. (1962), Possibility of subgrain rotation during recrystallization. J. Appl. Phys. 33, 2958-2965.

Liu, Y., P. Gilormini and P. Ponte Castañeda (2005), Homogenization estimates for texture evolution in halite. Tectonophysics, 406, 179-195.

Llorens, M-.G., P.D. Bons, A. Griera, E. Gomez-Rivas and L.A. Evans (2013a), Single layer folding in simple shear. J. Struct. Geol., 50, 209-220.

Llorens, M-.G., P.D. Bons, A. Griera and E. Gomez-Rivas (2013b), When do folds unfold during progressive shear?. Geology, 41, 563-566.

Llorens, M. -G., A. Griera, P. D. Bons, J. Roessiger, R. Lebensohn, L. A. Evans, and I. Weikusat (2016a), Dynamic recrystallisation of ice aggregates during co-axial viscoplastic deformation: a numerical approach. J. Glaciol. 62(232), 359-377.

Llorens, M. -G., A. Griera, P. D. Bons, R. Lebensohn, L. A. Evans, D. Jansen, and I. Weikusat. (2016b), Full-field predictions of bubble-free ice dynamic recrystallisation under simple shear conditions. Earth Planet. Sci. Lett., 450, 233-242.

Llorens, M. -G., A. Griera, F. Steinbach, P.D. Bons, E. Gomez-Rivas, D. Jansen, R. Lebensohn, and I. Weikusat (2017), Dynamic recrystallisation during deformation of polycrystalline ice: insights from numerical simulations. Phil. Trans. R. Soc. A, 375:20150346.

Mainprice, D., R. Hielscher, and H. Schaeben (2011), Calculating anisotropic physical properties from texture data using the MTEX open source package. Geol. Soc. London Spec. Publ. 360(1), 175-192.

Marques, F.O, J.-P. Burg, M. Armann and E. Martinho (2013), Rheology of synthetic polycrystalline halite in torsion. Tectonophysics, 583, 124-130.

Moldovan, D., D. Wolf, and S. R. Phillpot (2001), Theory of diffusion-accommodated grain rotation in columnar polycrystalline microstructures. Acta Mater. 49(17), 3521-3532.

Moldovan, D., D. Wolf, S. R. Phillpot, and A. J. Haslam (2002), Role of grain rotation during grain growth in a columnar microstructure by mesoscale simulation. Acta Mater. 50(13), 3397-3414.

Moulinec H. and P. Suquet (1995), A FFT-Based Numerical Method for Computing the Mechanical Properties of Composites from Images of their Microstructures. In: Pyrz, R. (Ed.), IUTAM Symposium on Microstructure-Property Interactions in Composite Materials. Solid Mechanics and its Applications, vol 37. Springer, Dordrecht.

Pantleon, W. (1997), On the evolution of disorientations in dislocation cell structures during plastic deformation. Mater. Sci. Eng. A234-236, 567-570

Pantleon, W. (1998), On the statistical origin of disorientations in dislocation structures. Acta Mater. 46(2), 451-456.

Pantleon, W. (2001), The evolution of disorientations for several types of boundaries. Mater. Sci. Eng. A319-321, 211-215.

Passchier, C. W., and R. A. J. Trouw (2005), Microtectonics. Springer, Berlin.

Pennock, G. M., and M. R. Drury (2005), Low angle subgrain misorientations in deformed NaCl. J. Microsc. 217, 130-137.

Pennock, G. M., M. R. Drury, P. W. Trimby, and C. J. Spiers (2002), Misorientation distributions in hot deformed NaCl using electron backscattered diffraction. J. Microsc. 205(3), 285-294.

Pennock, G. M., M. R. Drury, and C. J. Spiers (2004), Investigation of subgrain rotation recrystallization in dry polycrystalline NaCl. Mater. Sci. Forum 467-470, 597-602.

Pennock, G. M., M R. Drury, and C. J. Spiers (2005), The development of subgrain misorientations with strain in dry synthetic NaCl measured using EBSD. J. Struct. Geol. 27, 2159-2170.

Piazolo, S., P.D. Bons, M.W. Jessell, L. Evans, and C.W. Passchier (2002), Dominance of microstructural processes and their effect on microstructural development: insights from numerical modelling of dynamic recrystallization. Geol. Soc. Lon. Spec. Pub. 200, 149-170.

Piazolo, S., M.W. Jessell, D.J. Prior and P.D. Bons (2004), The integration of experimental in-situ EBSD observations and numerical simulations: a novel technique of microstructural process analysis. J. Microsc., 213, 273-284.

Pennock, G. M., M. R. Drury, C. J. Peach, and C. J. Spiers (2006), The influence of water on deformation microstructures and textures in synthetic NaCl measured using EBSD. J. Struct. Geol. 28, 588-601.

Randle, V. (1993), Microtexture investigation of the relationship between strain and anomalous grain growth. Philos. Mag. A 67.6, 1301-1313.

Randle, V., and O. Engler (2000), Introduction to Texture Analysis: Macrotexture, Microtexture and Orientation Mapping. Gorden & Breach Science Publications.

Read, W. T., and W. Shockley (1950), Dislocation models of crystal grain boundaries. Phys. Rev. 78.3, 275.

Schléder, Z., and J.L. Urai (2007), Deformation and recrystallization mechanisms in mylonitic shear zones in naturally deformed extrusive Eocene-Oligocene rocksalt from Eyvanekey plateau and Garmsar hills (central Iran). J. Struct. Geol. 29, 241-255.

Sethna, J. P., V. R. Coffman, and E. Demler (2003), Scaling in plasticity-induced cell-boundary microstructure: Fragmentation and rotational diffusion. Physical Review B 67, 184107.

Signorelli, J., and A. Tommasi (2015), Modeling the effect of subgrain rotation recrystallization on the evolution of olivine crystal preferred orientations in simple shear. Earth Planet. Sci. Lett. 430, 356-366.

Steinbach, F., P. D. Bons, A. Griera, D. Jansen, M.-G. Llorens, J. Roessiger, and I. Weikusat (2016), Strain localization and dynamic recrystallization in the ice-air aggregate: a numerical study. The Cryosphere 10, 3071-3089.

Stone, D. S., and T. Plookphol (2004), Similarity and scaling in creep and load relaxation of single-crystal halite (NaCl). J. Geophys. Res. 109, B12201.

Trimby, P. W., M.R. Drury, and C. J. Spiers (2000), Recognising the crystallographic signature of recrystallization processes in deformed rocks: a study of experimentally deformed rocksalt. J. Struct, Geol 22, 1609-1620.

Urai, J.L., W. D. Means, and G. S. Lister (1986), Dynamic recrystallization of minerals. In: Hoobs, B. (Ed.), Mineral and Rock Deformation: Laboratory Studies: The Paterson Volume, pp. 161-199.

Urai, J., Z. Schléder, C. Spiers, and P. A. Kukla (2008), Flow and Transport Properties of Salt Rocks. In: Littke, R., Bayer, U., Gajewski, D., Nelskamp, S. (Eds.), Dynamics of complex intracontinental basins: The Central European Basin System. Springer-Verlag, Berlin Heidelberg, 277-290.

Wang, L., S. Blaha, T. Kawazoe, N. Miyajima, and T. Katsura (2017), Identical activation volumes of dislocation mobility in the [100](010) and [001](010) slip systems in natural olivine. Geophys. Res. Lett. 44, 2687-2692.

Weiss, L. E., and H. R. Wenk (1985), Preferred orientation in deformed metals and rocks: an introduction to modern texture analysis. Academic Press, London.

Wenk, H. -R., G. R. Canova, A. Molinari, and H. Mecking (1989), Texture development in halite: comparison of Taylor model and self-consistent theory. Acta Metall. 37, 2017-2029.

Wenk, H. -R., M. Armann, L. Burlini, K. Kunze, and M. Bortolotti (2009), Large strain shearing of halite: Experimental and theoretical evidence for dynamic texture changes. Earth and Planetary Science Letters 280, 205-210.

Supporting Information for

Subgrain rotation recrystallization during shearing: insights from full-field numerical simulations of halite polycrystals

E. Gomez-Rivas[1], A. Griera[2], M. -G. Llorens[3], P. D. Bons[3], R. A. Lebensohn[4], and S. Piazolo[5]

[1]School of Geosciences, King's College, University of Aberdeen, Aberdeen AB24 3UE, United Kingdom

[2]Departament de Geologia, Universitat Autònoma de Barcelona, 08193 Bellaterra (Cerdanyola del Vallès), Spain

[3]Department of Geosciences, Eberhard Karls University of Tübingen, Wilhelmstr. 56, 72074 Tübingen, Germany

[4]Materials Science and Technology Division, Los Alamos National Laboratory, Los Alamos NM 87545, USA

[5]School of Earth and Environment, University of Leeds, Leeds LS2 9JT, United Kingdom

Introduction

This supporting information provides (i) a more detailed description of the ELLE-recovery approach, including **Figure S1** (see section 2.2 for an introduction), (ii) sketches showing the basic ELLE data structure and illustrating how the repositioning routine works (**Figure S2**), (iii) movies of two numerical experiments (**Movie ms01** and **Movie ms01**), (iv) a figure to demonstrate the influence of the recovery time step with respect to the deformation time step (**Figure S3**), in order to prove that the approach of applying numerical processes sequentially is appropriate, and, finally, (v) a figure displaying maps of the equivalent stress (**Figure S4**).

Detailed description of the physical basis for the conceptual model of the ELLE-recovery approach

A more detailed description of the ELLE-recovery process is given here, in order to complement the explanation of section 2.2. As mentioned in that section, the ELLE-recovery process used here is based on a slight modification of the method proposed by *Borthwick et al.* [2014]. The approach is conceptually based on the reduction of internal stored energy (i.e., misorientation) of the microstructure following a series of equations that rotate the crystal lattice in order to minimize the boundary energy between crystallites (or *unodes*). This results in the development of subgrains with more homogenous lattice orientations and the re-arrangement or disappearance of subgrain boundaries. The approach assumes that the distortion of the crystal structure is due to the presence of geometrically necessary dislocations (GNDs). For a certain angle of misorientation (θ) it is possible to calculate the density (ρ) of GNDs to unbend the lattice distortion (*Ashby [1970]*). This density is a function of the misorientation angle (θ), the distance (δx) over which the rotation occurs, and the Burgers vector (b) (which accounts for the magnitude of lattice distortion):

$$\rho_i = \frac{\theta_i}{\delta x_i b_i} \qquad [A1]$$

where the subscript *i* refers to the dislocation type under consideration with a rotation axis that lies on the slip plane (*Borthwick et al.* [2014]). The summation of the rotation of individual dislocation systems allows applying any arbitrary small angle of rotation. The boundary energy (φ) of a subgrain with a misorientation angle θ can be calculated assuming a simple tilt-boundary geometry (*Read and Shockley [1950]*):

$$\varphi_{(\theta)} = \frac{\varphi_m \theta}{\theta_m \left(1 - \ln(\theta / \theta_m)\right)} \qquad \text{[A2]}$$

where θ_m is the critical misorientation angle for the transition between low-angle (or sub-grain) boundaries and high-angle grain boundaries at which the boundary energy is φ_m.

Following the approach by *Borthwick et al.* [2014], we assume here that the rotation rate of a subgrain is proportional to the torque (Q) generated by the change of boundary energy associated with the misorientation reduction (as previously proposed by e.g., *Li* [1962]; *Erb and Gleiter* [1979]; *Randle* [1993] or *Moldovan et al.* [2002]). We consider a linear relationship between the angular velocity ω and a driving torque Q, in a similar way as other authors propose for grain boundary migration, where the velocity is proportional to a driving force (i.e., $v = M\Delta F$; e.g., *Urai et al.* [1986]),

$$\omega = M'Q \qquad \text{[A3]}$$

where *M'* is the rotational mobility (*Moldovan et al.* [2002]). A derivation of *M'* assuming a viscous rheology is shown in the following paragraphs. Following *Borthwick et al.* [2014], the torque acting on a group of data points (the rectangular grid of *unodes* that are treated as crystallites) of neighborhood size *N* with datum point *i* in the center is given by:

$$Q = \sum_{j=0}^{N} l \, d\varphi_{ij} \big/ d\theta_{ij} \qquad \text{[A4]}$$

where *l* is the boundary length between the datum point *i* and the neighboring datum point *j*, θ_{ij} is the misorientation angle across the boundary between these two data points, and φ_{ij} is the surface energy. This relationship assumes that the torque *Q* is calculated with respect to an axis through the mass center of data point *i*. During this calculation only energy of low-angle grain boundaries is taken into account.

The tensor **M** accounts for the rotation between two neighbor data points with orientations g_i and gj (with rotation matrices **R**i and **R**j, respectively):

$$\mathbf{M} = \mathbf{R}_i \times \mathbf{R}_j^{-1} \qquad \text{[A5]}$$

This tensor allows calculating the misorientation angle between such points (e.g., *Weiss and Wenk* [1985]):

$$\theta = \arccos\left[(tr(\mathbf{M}) - 1)/2\right] \qquad \text{[A6]}$$

For calculating the minimum misorientation angle (θ) between two neighboring data points, equivalent rotations need to be considered for materials with cubic crystal symmetry such as halite. For cubic materials, the 24 symmetry operators are applied and the rotation tensor that yields a minimum θ is utilized (*Bunge* [1985]). In order to calculate the misorientation angle, and therefore the boundary energy, only first-neighboring *unodes* that belong to the same grain are taken into account (i.e., when the boundary angle between the pivot *unode* and the neighbor *unode* is lower than the critical misorientation angle (θ_m) for the transition between low-angle and high-angle grain boundaries).

The recovery process in ELLE assumes that each *unode* is a potential subgrain and thus the boundary energy and misorientation are minimized by their rotation. The algorithm starts by choosing a random *unode* and finding the first-neighboring *unodes* that belong to the same grain. The crystal orientation of the reference *unode* is rotated a small angle (0.1°) using a set of pre-defined crystal directions. For halite, we consider a linear independent basis defined by [100], [010] and [001] crystal directions as rotation axes. The combination of this set of axes is able to define the entire rotation axis related to the slip systems used in the viscoplastic approach. The orientation of the reference *unode* is rotated towards the value that results in the maximum reduction in energy, while the crystal orientation is not changed if trial rotations result in an increase of energy of the neighborhood. This procedure is repeated for each *unode* in random order every time step. The numerical predictions were verified by *Borthwick et al.* [2014] using results from intracrystalline evolution during annealing experiments of deformed single salt crystals (*Borthwick and Piazolo* [2010]).

There are several slight differences between the approach used in our study and that of *Borthwick et al.* [2014]. While these authors used pre-fixed rotation rates (a reference value of 0.2°), in our approach the rotation rate is calculated using equations A4 and A5 and, therefore, the rotation rate depends on the boundary energy reduction. Following equation A1, the reduction of dislocations is proportional to the decrease in misorientation angle due to lattice rotation. *Borthwick et al.* [2014] utilized a normalized value of rotation mobility *M'* instead of a relationship between *M'* and the material properties. As a first approximation, here we propose a relationship between *M'* and the effective viscosity of the material (see below). In *Borthwick et al.* [2014] several relative activities of the pre-defined rotation axes were used in order to simulate variable activities of the different slip systems. Here, we have considered that no rotation axis dominates and that all rotation axes have the same rotation mobility *M'*.

To estimate the rotation mobility *M'* as a viscous parameter, we assume that each *unode* is a small square crystallite of dimensions $l \cdot l \cdot L$, where L is in the third dimension. The lattice inside this volume has orientation g_i and the lattice orientation g_j in the four neighboring crystallites may be different. We treat the boundaries between the crystallites as subgrain boundaries with surface energy φ_{ij} (J/m^2), which is a function of the angular mismatch between the orientations g_i and g_j. In the explanation here, we simplify the function with the assumption that all neighboring crystallites have the same lattice orientation, in which case the total boundary energy of one *unode* system (E_i) is

$$E_i = 4lL\varphi_{ij} \tag{A7}$$

In the actual algorithm, the angular mismatches with each individual neighbor are taken into account.

A rotation of the lattice (i.e., a change in angle θ of the initial orientation g_i) modifies the local energy E_i of the system. We assume that the rotation is achieved by simple shear of the square crystallite. This is actually appropriate, as the rotation is achieved by dislocations that glide from one side to the other. Let's define x as the position of one side relative to the opposite side. A change in x thus entails simple shear. The change in E_i as a function of x can be described with:

$$\frac{dE_i}{dx} = \frac{d\left(4lL\varphi_{ij}\right)}{dx} = 4lL\left(\frac{d\varphi_{ij}}{dx}\right) = 4lL\left(\frac{d\varphi_{ij}}{d\theta}\right)\left(\frac{d\theta}{dx}\right) \tag{A8}$$

Taking a small rotation $\theta \sim 0^\circ$ of the crystallite lattice, we can write θ as

$$\theta = \tan^{-1}\left(\frac{x}{l}\right) \approx \frac{x}{l} \tag{A9}$$

when x and θ are small increments. If Eq. A9 is derived with respect to x, it follows that $d\theta/dx \sim l^{-1}$, which can be inserted in Eq. A8:

$$\frac{dE_i}{dx} = 4L\left(\frac{d\varphi_{ij}}{d\theta}\right) \tag{A10}$$

dE/dx is actually the force acting on the sides of the crystallite, driving the shearing. From this we can determine the shear stress (τ), which is the force acting on the total lateral surface area of the crystallite, which is $4\cdot l\cdot L$, to obtain:

$$\tau = \frac{1}{4lL}\left(\frac{dE_i}{dx}\right) = \frac{1}{l}\left(\frac{d\varphi_{ij}}{d\theta}\right) \tag{A11}$$

For a linear viscous material, the shear strain rate ($\dot{\gamma}$) is related to the shear stress by the viscosity (η), which we assume to be constant. Furthermore, as the rotation rate ($\dot{\omega}$) is half of the shear strain rate ($\dot{\omega} = \dot{\gamma}/2$), we obtain:

$$\dot{\omega} = \frac{\dot{\gamma}}{2} = \frac{\tau}{2\eta} = \frac{1}{2l\eta}\left(\frac{d\varphi_{ij}}{d\theta}\right) \tag{A12}$$

In the recovery approach, the rotation rate is calculated as a linear relation between a driving torque Q' and a rotational mobility M' (equations A10 and A11):

$$Q = 4l\left(\frac{d\varphi_{ij}}{d\theta}\right) \tag{A13}$$

and

$$\dot{\omega} = MQ = 4Ml\left(\frac{d\varphi_{ij}}{d\theta}\right) \tag{A14}$$

Combining Eqs. A12 and A14, the rotation mobility *M'* can be expressed as a function of the viscosity of the material and the size of the crystallite (length size of *unodes*):

$$\dot{\omega} = 4M'l\left(\frac{d\varphi_{ij}}{d\theta}\right) = \frac{1}{2l\eta}\left(\frac{d\varphi_{ij}}{d\theta}\right) \Leftrightarrow M' = \frac{1}{8l^2\eta} \tag{A15}$$

Therefore from equation A15, the rotational mobility *M'* can be calculated if the effective viscosity of the material is known.

Calculation of kinetics of recovery

The kinetics of recovery dθ/dt associated with the misorientation reduction carried out by the ELLE recovery process can be calculated using a second-order rate equation, in a similar way as other authors use for constraining the dislocation evolution during annealing experiments (e.g., *Farla et al.* [2010]):

$$\frac{d\theta}{dt} = -\theta^2 k_\theta \tag{A16}$$

where k_θ is the rate constant. This equation integrates to

$$\frac{1}{\theta_f} - \frac{1}{\theta_i} = k_\theta t \tag{A17}$$

where t is time and θ_i and θ_f are the initial and final misorientation angles, respectively. The progressive decrease of k_θ with increasing strain can be visualized in Fig. S1, with values of log(k_θ) ranging from -6 to -7 during early deformation stages, and between -9 and -10 at the end of the simulation time. The difference between the three recovery scenarios (SGC1, SGC10 and SGC25) is only of one order of magnitude. The progressive reduction of k_θ is coherent with a continuous increase of high-angle boundaries and grain size reduction. Note that only low-angle boundaries are taken into account for the calculations. Using annealing experiments of salt single crystals, *Borthwick and Piazolo* [2010] observed variations of the misorientation-change rate along subgrain boundaries of up to a maximum 0.3° per hour. Changes of the rate constant k_θ between -4 and -5 can be inferred from their figure 9. These values are notably higher than those observed in our simulations, but our values are for the whole area of the model while the data of *Borthwick and Piazolo* [2010] are restricted to a selection of grain boundaries.

Our calculations consider the whole model area, with corresponds to 0.01 m². Using this value, an equivalent constant *k* relating the kinetics of recovery of dislocation density can also be

calculated. For our specific simulations, this constant ranges between -18 and -22 m^2/s. Since there are no published equivalent values from halite experiments we can only compare our data with that from olivine. Our values are slightly lower than those reported from annealing experiments of olivine aggregates (e.g., *Farla et al.* [2010]; *Wang et al.* [2017], which range between -17 and -19 m^2/s). Values obtained from experiments are acquired with oxidative decoration techniques and removing high-angle boundaries, while our calculation is based on the local misorientation field (without taking into account high-angle grain boundaries). It is worth noting that dislocation density can be calculated from misorientation using Eq. (A1) assuming a tilt boundary.
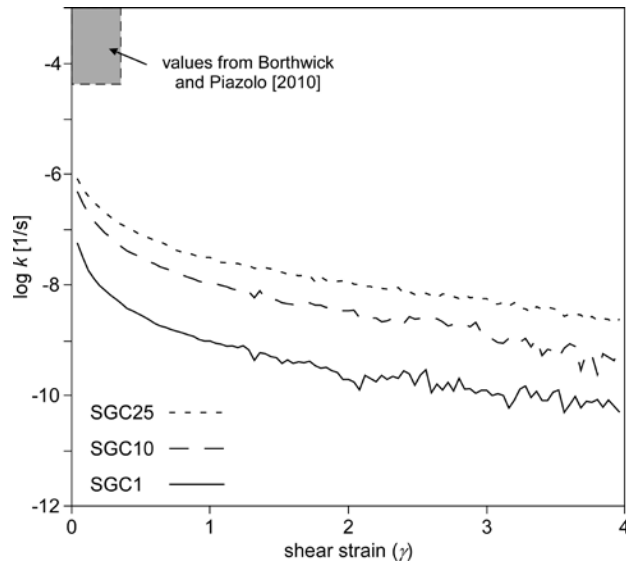

Figure S1. Evolution of an equivalent constant *k* (measured in [1/s]) that accounts for the kinetics of recovery of misorientation for our simulations with recovery SGC1, SGC10 and SGC25. The ranges of values obtained from the experiments by *Borthwich and Piazolo* [2010] are also indicated.

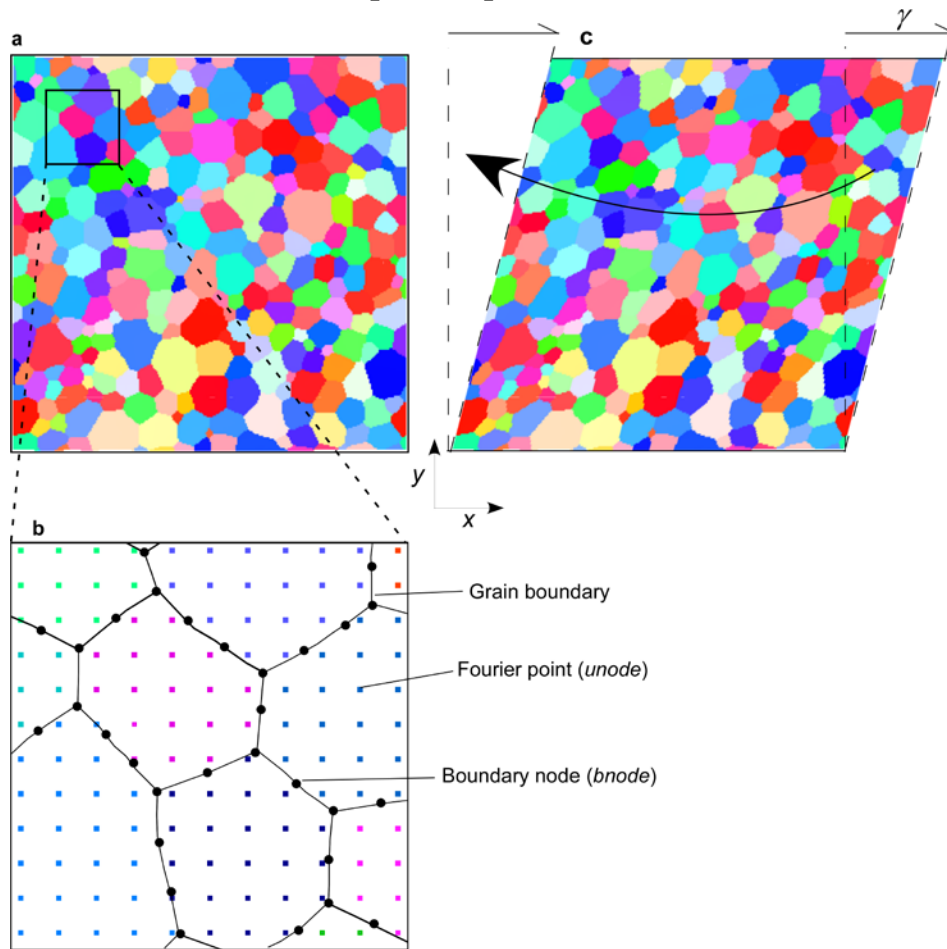## ELLE data structure, simulation setup and reposition routine

Figure S2. (a,b) Basic data structure and setup of simulations. The ELLE structure includes two layers of data: boundary nodes (*bnodes*) that define grains (as polygons) and a regular mesh of unconnected nodes (*unodes*) that store crystal orientations and dislocation density and act as Fourier points or crystallites for VPFFT calculations. (c) A routine repositions the model back into a 1x1 unit cell after each deformation time square in order to allow visualizing the microstructure even when high shear strain is reached.

Simulation movies

Movie ms01. Movie of the experiment SGC0 (with zero steps of the subgrain coarsening process per deformation step) up to a shear strain of $\gamma=4$. The main window shows the evolution of the orientation and grain boundary map with progressive deformation. Stereograms display pole figures of the CPO evolution, using equal area projection. The progress of the model bounding box without reposition in simple shear is displayed at the lower part of the movie (see methods section for further explanations).

Movie ms02. Movie of the experiment SGC10 (with ten steps of the subgrain coarsening process per deformation step) up to a shear strain of $\gamma=4$. The main window shows the evolution of the orientation and grain boundary map with progressive deformation. Stereograms display pole figures of the CPO evolution, using equal area projection. The progress of the model bounding box without reposition in simple shear is displayed at the lower part of the movie (see methods section for further explanations).
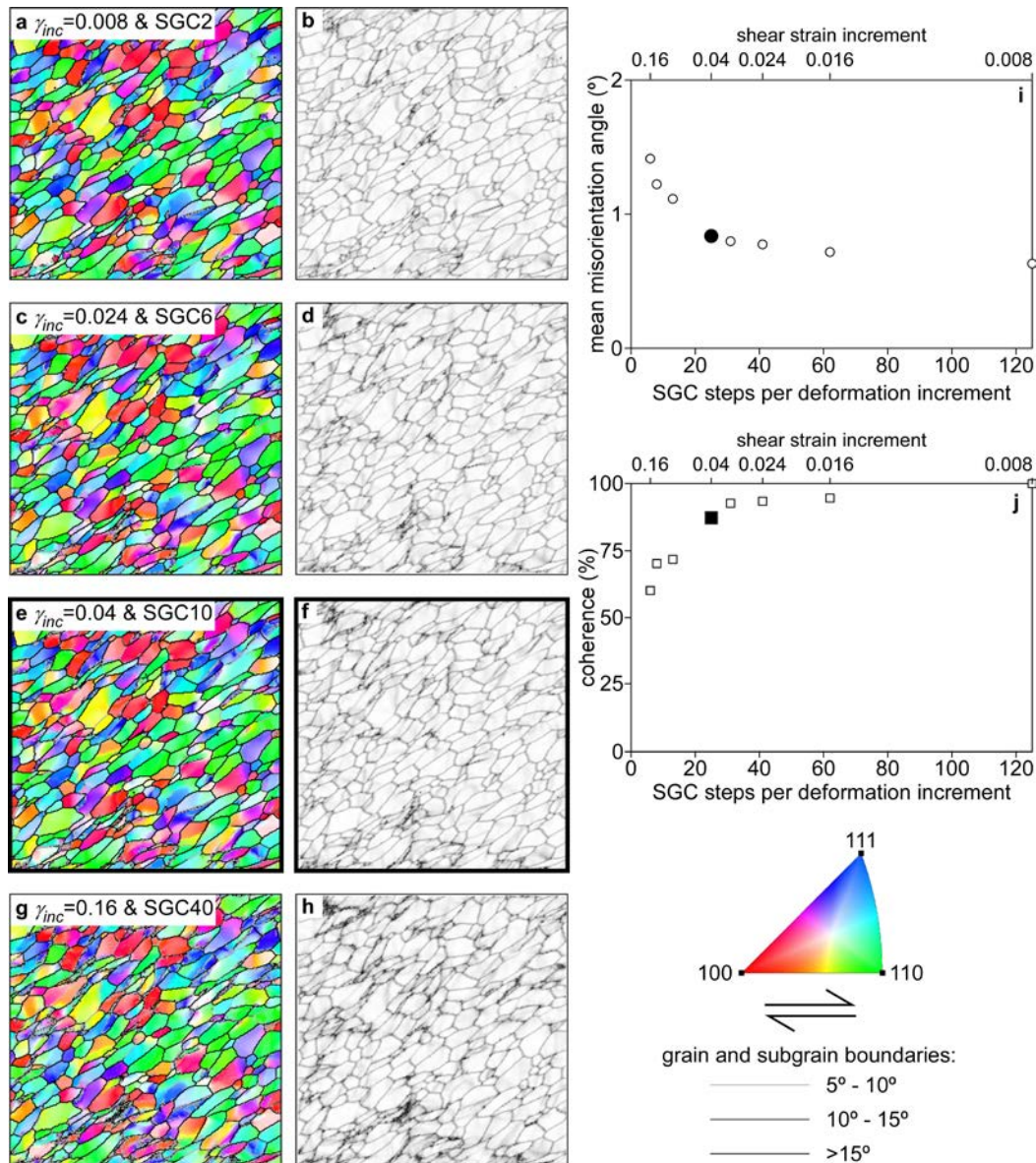
Evaluation of influence of time step size

Figure S3. Comparison of results of numerical experiments of the model SGC10 varying the ration between incremental shear strain (γ_{inc}) and the number of recovery (subgrain coarsening, SGC) steps per deformation increment, at a finite shear strain of γ=1. The balance between different configurations to achieve 10 SGC steps for a shear strain increment of γ_{inc}=0.04 is tested: (a,c,e,g) display orientation and grain boundary maps of the different runs, while (b,d,f,h) show subgrain misorientation maps (with black representing 15°). The trace of the shear plane is horizontal and the shear sense is dextral in these figures. The maps corresponding to the chosen configuration (SGC10 for γ_{inc}=0.04) are marked using a thicker frame. (i) shows the variation of the geometric mean of misorientations per grain for the different configurations at a finite shear strain of γ=1, and demonstrates that the difference between the two extreme models is less than 0.8°, with only 0.17° between the chosen configuration (solid circle) and that with more SGC steps. (j) is a plot of the coherence (in percentage) of the resulting misorientations for each configuration with respect to the model with the highest number of SGC steps (125). This is calculated as the deviation of the distribution of misorientations from that model. The results show that the coherence of the chosen configuration (SGC10 for γ_{inc}=0.04, solid square) is >87% with respect to the test with SGC125 for γ_{inc}=0.008, at a finite strain of γ=1.
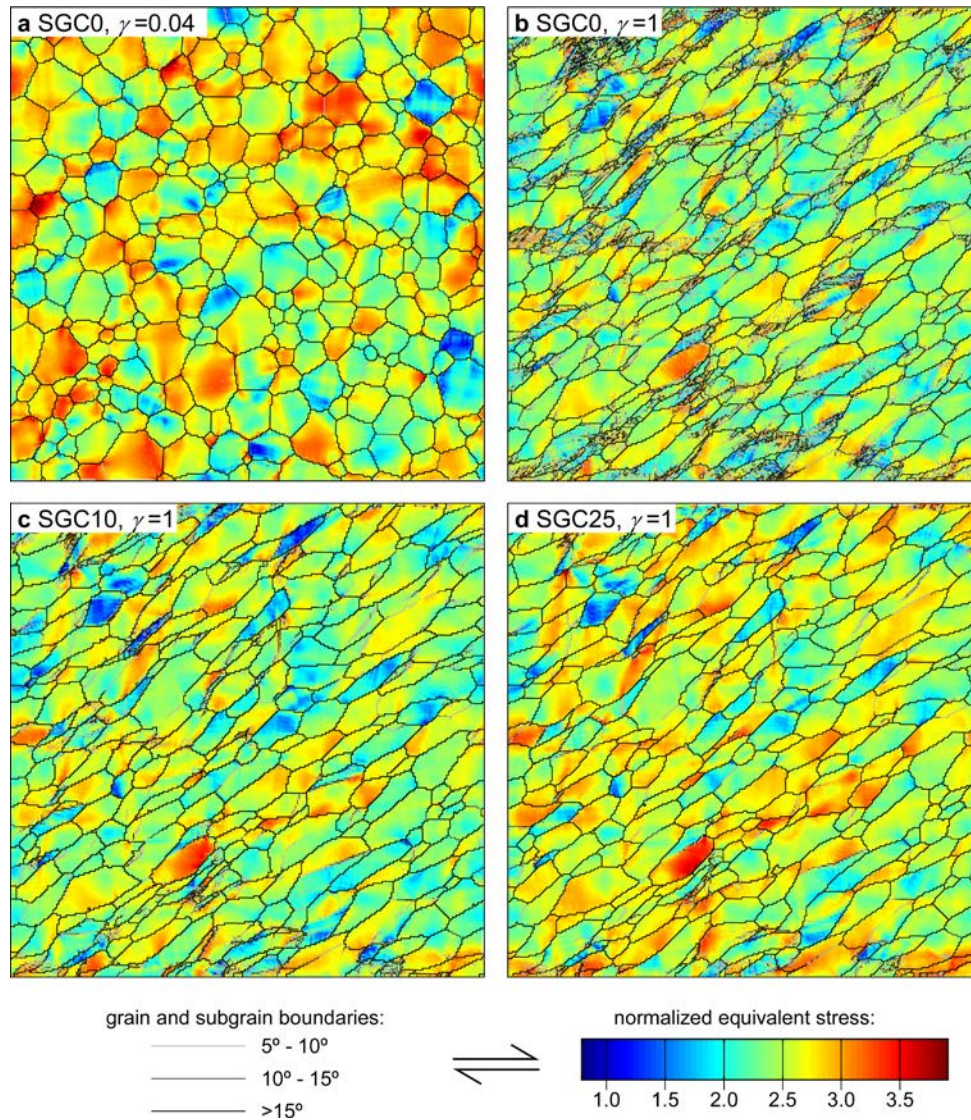
Stress distribution

Figure S4. Map of equivalent stress (normalized according to the strain rate and strength) (a) for the SGC0 simulation after a shear strain of $\gamma=0.04$ and (b) the SGC0, (c) SGC10 and (d) SGC25 models after a shear strain of $\gamma=1$. As expected, stress increases in areas where crystal orientations differ. Intracrystalline recovery can lead to an increase of stress concentrations in certain areas because it reduces the formation of new grains associated with rotation recrystallization.